

# Compositions and Interior Structures of the Large Moons of Uranus and Implications for Future Spacecraft Observations

Julie Claire Castillo<sup>1</sup>, Benjamin P Weiss<sup>2</sup>, Chloe B Beddingfield<sup>3</sup>, John B. Biersteker<sup>2</sup>, Richard J Cartwright<sup>4</sup>, Allison Goode<sup>2</sup>, Mohit Melwani Daswani<sup>5</sup>, and Marc Neveu<sup>6</sup>

<sup>1</sup>Jet Propulsion Laboratory

<sup>2</sup>Massachusetts Institute of Technology

<sup>3</sup>The SETI Institute / NASA Ames Research Center

<sup>4</sup>The SETI Institute

<sup>5</sup>Unknown

<sup>6</sup>Goddard Space Flight Center/University of Maryland

November 23, 2022

## Abstract

The five large moons of Uranus are important targets for future spacecraft missions. To motivate and inform the exploration of these moons, we model their internal evolution, present-day physical structures, and geochemical and geophysical signatures that may be measured by spacecraft. We predict that if the moons preserved liquid until present, it is likely in the form of residual oceans less than 30 km thick in Ariel, Umbriel, Titania, and Oberon. The preservation of liquid strongly depends on material properties and, potentially, on dynamical circumstances that are unknown. Miranda is unlikely to preserve liquid until present unless it experienced tidal heating a few tens of million years ago. The triaxial shapes estimated from Voyager 2 data for Miranda and Ariel further support the prospect that these moons are internally differentiated with a rocky core and icy shell. We find that since the thin residual layers may be hypersaline, their induced magnetic fields could be detectable by future spacecraft-based magnetometers. However, if the ocean is maintained primarily by ammonia, and thus well below the water freezing point, then its electrical conductivity may be too small to be detectable by spacecraft. Lastly, our calculated tidal Love number ( $k_2$ ) and dissipation factor ( $Q$ ) are consistent with the  $Q/k_2$  values previously inferred from dynamical evolution models. In particular, we find that the low  $Q/k_2$  estimated for Titania supports the hypothesis that Titania currently holds an ocean.

## Hosted file

essoar.10511640.1.docx available at <https://authorea.com/users/62385/articles/600724-compositions-and-interior-structures-of-the-large-moons-of-uranus-and-implications-for-future-spacecraft-observations>

# Compositions and Interior Structures of the Large Moons of Uranus and Implications for Future Spacecraft Observations

Julie Castillo-Rogez<sup>1</sup>, Benjamin Weiss<sup>1,2</sup>, Chloe Beddingfield<sup>3,4</sup>, John Biersteker<sup>2</sup>, Richard Cartwright<sup>3</sup>, Allison Goode<sup>2</sup>, Mohit Melwani Daswani<sup>1</sup>, Marc Neveu<sup>5,6</sup>

1. Jet Propulsion Laboratory, California Institute of Technology, Pasadena, CA, USA.
2. Department of Earth, Atmospheric and Planetary Sciences, Massachusetts Institute of Technology (MIT), Cambridge, MA, USA.
3. SETI Institute, Mountain View, CA, USA.
4. NASA Ames Research Center, Mountain View, CA, USA.
5. University of Maryland, College Park, MD, USA.
6. NASA Goddard Space Flight Center, Greenbelt, MD, USA.

## Key Points

- Most of the major Uranian moons may host a residual ocean a few tens of kilometers thick at present, except for Miranda.
- If the ocean temperature is seer
- These models represent a baseline for the formulation of moon observations with the Uranus Orbiter and Probe.

## Abstract

The five large moons of Uranus are important targets for future spacecraft missions. To motivate and inform the exploration of these moons, we model their internal evolution, present-day physical structures, and geochemical and geophysical signatures that may be measured by spacecraft. We predict that if the moons preserved liquid until present, it is likely in the form of residual oceans less than 30 km thick in Ariel, Umbriel, Titania, and Oberon. The preservation of liquid strongly depends on material properties and, potentially, on dynamical circumstances that are unknown. Miranda is unlikely to preserve liquid until present unless it experienced tidal heating a few tens of million years ago. The triaxial shapes estimated from Voyager 2 data for Miranda and Ariel further support the prospect that these moons are internally differentiated with a rocky core and icy shell. We find that since the thin residual layers may be hypersaline, their induced magnetic fields could be detectable by future spacecraft-based magnetometers. However, if the ocean is maintained primarily by ammonia, and thus well below the water freezing point, then its electrical conductivity may be too small to be detectable by spacecraft. Lastly, our calculated tidal Love number ( $k_2$ ) and dissipation factor ( $Q$ ) are consistent with the  $Q/k_2$  values previously inferred from dynamical evolution models. In particular,

we find that the low  $Q/k_2$  estimated for Titania supports the hypothesis that Titania currently holds an ocean.

### Plain Language Summary

The major moons of Uranus, Miranda, Ariel, Umbriel, Titania, and Oberon, are interesting targets for a future space mission because they might host liquid at present. Studying these bodies would help address the extent of habitable environments in the outer solar system. We model their thermal, physical, and chemical evolution. Because their heat budget is limited, with little or no tidal heating at present, we find that most of the moons can preserve only a few tens of kilometers of liquid until present. Furthermore, if the oceans are maintained by antifreeze, such as ammonia and chlorides, then their electrical conductivities may be close to zero. In this case, the detection of a magnetic field induced in these oceans would be challenging. We explore additional geophysical, as well as compositional, observations that would reveal the existence of a deep ocean in these moons. None of the scenarios studied yields residual liquid in Miranda at present. Our simulations are consistent with constraints on the dissipative properties of the moons inferred from dynamical evolution models.

### 1. Study Motivations and Goals

The last decade has seen a growing interest in exploration of the ice giant systems, recently culminating with the prioritization of a Uranus Orbiter and Probe (UOP) in the Planetary Science and Astrobiology Decadal Survey for 2023-2032 (Origins, Worlds, Life, NASEM 2022). This concept includes a strong focus on understanding the evolution and current state of Uranus’ large five moons: Miranda, Ariel, Umbriel, Titania, and Oberon. In particular, UOP would test whether some of these moons are ocean worlds (i.e., host deep, global-scale oceans at present) (see Roadmap to Ocean Worlds, Hendrix et al. 2019).

There have been few studies about the internal evolution of the large Uranian moons. Hussmann et al. (2006) and, more recently, Bierson and Nimmo (2022) predicted that Titania and Oberon could contain thick oceans, whereas Ariel, Umbriel, and Miranda would be frozen at present. These studies concluded that deep oceans, if present, would be maintained by the presence of ammonia, an antifreeze expected in most icy moons (e.g., Kargel 1998). However, these models suffer from two caveats. Firstly, accreted ammonia can speciate into ammonium, which can eventually be removed from the system by precipitation as salts (Marion et al. 2012). Hence, ammonia’s antifreeze role is significantly diminished. Secondly, due to the temperature dependence of electrical conductivity (EC), cold oceans sustained by antifreeze may have a very weak or even near-zero EC.

Here we revisit the evolution, composition and structure of the large Uranian moons, motivated by multiple recent advances: surface chemistry and geology (in particular, heat flow estimates), revised dynamical models, and reinterpretation of shape data. Furthermore, we leverage knowledge gained on the geochemistry and geophysics of icy bodies comparable in size to the Uranian moons

(i.e., 100-1000 km in diameter) (Figure 1) derived from recent observations of Enceladus and other moons of Saturn by Cassini, Pluto and Charon by New Horizons, and Ceres by Dawn.

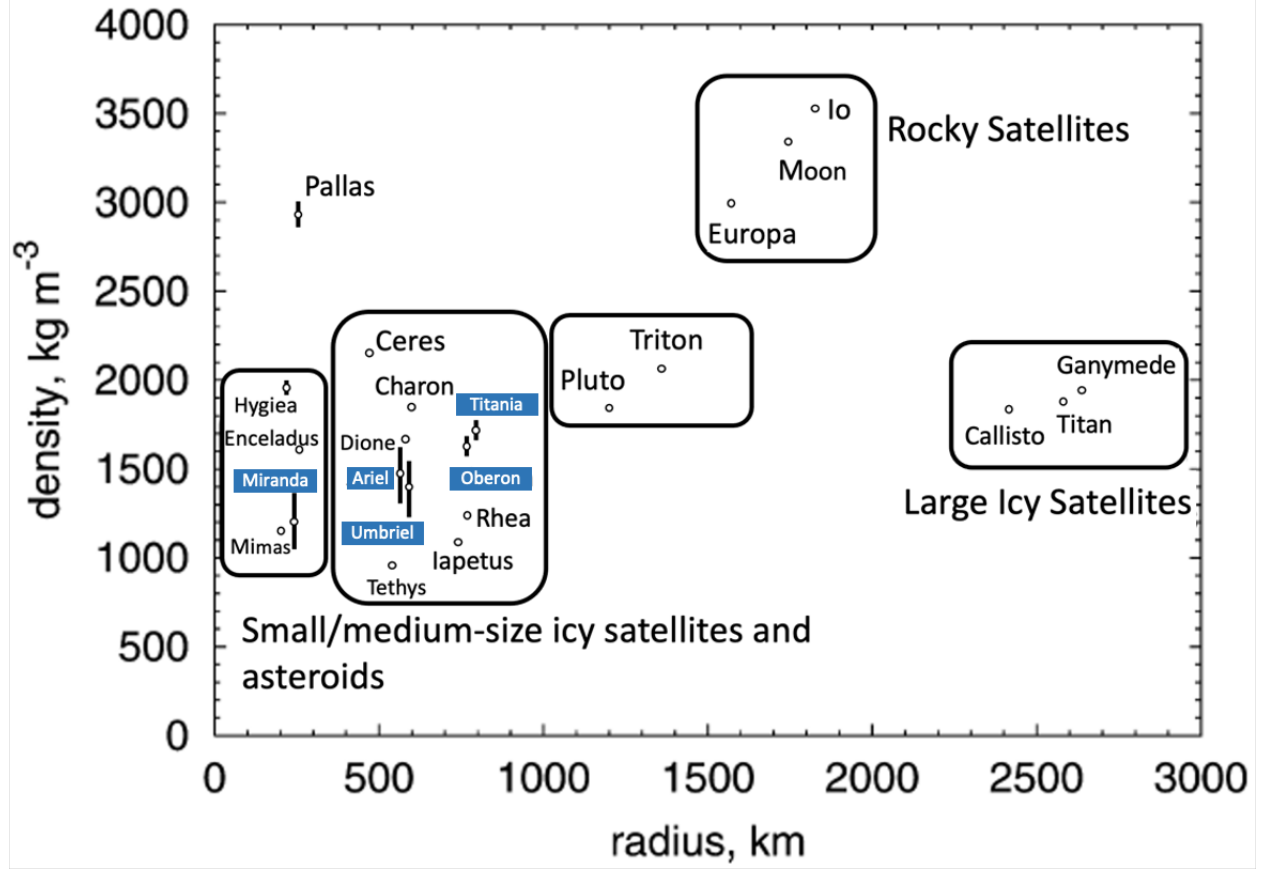


Figure 1. Densities and mean radii of the Uranian moons compared to those of other large moons and dwarf planets. Miranda has a low density similar to Saturn’s moon Mimas, whereas the densities of the other Uranian moons are more similar to Saturn’s moons Dione and Rhea. After Hussman et al. (2006).

The goals of this study are to (1) to predict the extent of differentiation for the moons based on various heat budget scenarios; (2) assess the conditions for the preservation of deep oceans in the moons until present for various reference temperatures; (3) quantify physical parameters that can be observed by a future spacecraft mission aiming at understanding the moon evolution and current states.

Available observational constraints on the large moon’s surface and interior properties are summarized in Section 2. The various models used in this study to model thermal evolution and physical parameters are summarized in Section 3

with their input parameters. The resulting interior structures are presented in Section 4. Alternative assumptions on the moon’s origins and evolution pathways are addressed in Section 5. These results serve as a basis for observational quantifying observation requirements in Section 6. The primary products of this study are a range of possible interior structures and associated estimates of the degree 2 gravity coefficients, triaxial shape, electrical conductivity estimates, and induced magnetic field predictions (Section 6). These can serve as a reference for designing future mission investigations targeting these moons in order to assess the extent of differentiation of their interiors and the conditions for detecting an ocean.

### 1. Observational Constraints

We review constraints on the large Uranian moons’ surface compositions, when available and inferences from geological analyses (crater-based geochronology pointing to partial resurfacing and heat flow estimates from flexure analysis) and dynamical modeling. The physical and dynamical properties of the large Uranian moons are gathered in Table 1.

Table 1. Key physical and dynamical properties of Uranus’ large moons. References for radii and densities are Archinal et al. (2018) and Jacobson (2014). Mean values are used in the simulations presented in this paper. Dynamical properties are provided by *ssd.jpl.nasa.gov* based on Jacobson (2014). References for temperature are Hanel et al. (1986), Janes and Melosh (1988), and Grundy et al. (2006).  $Q/k_2$  constraints are from Cuk et al. (2020). Power for obliquity-driven tides in the ocean is taken from Chen et al. (2014). Eccentricity-driven tides in the ocean produce several orders of magnitude less heat based on the latter study.

<b>Properties</b>	<b>Miranda</b>	<b>Ariel</b>	<b>Umbriel</b>	<b>Titania</b>	<b>Oberon</b>
<b>Mean</b>	$\pm 0.7$	$\pm 0.6$	$\pm 2.8$	$\pm 1.8$	$\pm 2.6$
<b>Radius, <math>R</math> (km)</b>					
<b>(1- )</b>					
<b>Mean</b>	$\pm 0.053$	$\pm 0.026$	$\pm 0.041$	$\pm 0.032$	$\pm 0.05$
<b>Density (<math>\text{kg/m}^3</math>)</b>					
<b>(1- )</b>					
<b>Suburanian</b>	$\pm 0.6$	$\pm 0.9$	Not	Not	Not
<b>Equato- rial</b>			available	available	available
<b>Radius, <math>a</math> (km)</b>					
<b>(1- )</b>					

Along-Orbit Equatorial Radius, $b$ (km) (1- )	$\pm 0.9$	$\pm 0.6$	Not available	Not available	Not available
Polar Radius, $c$ (km) (1- )	$\pm 1.2$	$\pm 1.0$	Not available	Not available	Not available
Mean Surface Temperature (K)	-70	-70			-80
Central Pressure (MPa)					
Semi-Major Axis, $D$ (km)	858	930	982	282	449
Orbital Eccentricity, $e$					
Orbital Inclination, $i$ ( $^{\circ}$ )					
Rotation and Orbital Period $n$ , $=2/n$ (hours)					
Radioactive decay power at present (GW)	$\sim 0.8$	$\sim 2.8$	$\sim 2.8$	$\sim 8.4$	$\sim 7.7$

$(R)^5 e^2 / G$	$\sim 7.2$	$\sim 28.8$	$\sim 26.5$	$\sim 0.3$	
(GW)					
For current values of $e$ and (above)					
<b>Solid Body Power from Ec- centricity Tides at Present (GW)</b>	$\sim 8 \times 10^{-3}$	$\sim 3 \times 10^{-2}$	$\sim 3 \times 10^{-2}$	$\sim 3 \times 10^{-4}$	$\sim 4 \times 10^{-4}$
Assuming $k_2/Q =$ $10^{-4}$					
<b>Maximum Power from Obliquity Tides in Ocean at Present (GW)</b>	$3 \times 10^{-4}$	$\sim 5 \times 10^{-8}$	$\sim 2 \times 10^{-6}$	$\sim 10^{-4}$	$\sim 5 \times 10^{-3}$
(Chen et al. 2014)					
$k_2/Q$	$-5 - 10^{-6}$	$-4 - 10^{-5}$	$-4 - 10^{-5}$	$> 10^{-3}$	$-4$
Average, based on orbital parameter evolution since $\sim 1$ Ga					

### 2.1 Constraints on the Interiors of Miranda and Ariel from Voyager 2 Shape Data

We explore the information confirmed in the ellipsoidal shape (equatorial radii,  $a$  and  $b$ , and polar radius  $c$ , with  $a > b > c$ ) published by Archinal et al. (2018). Figure 2 presents values of  $a$ ,  $b$ , and  $c$  for different interior structures (differentiated and undifferentiated) assuming hydrostatic equilibrium (e.g., Zharkov et al. 1985, see also Section 6.1). These estimates suggest that the radii inferred from

Voyager images are consistent to  $\sim 2\%$  with differentiated interiors for Ariel and Miranda. To the best of our knowledge, this finding has never been reported. In the case of Miranda, it would support a model where Miranda's interior is differentiated in a dense rocky core and low-density shell. The measurement uncertainty and the weak dependency of  $(a-c)$  on the core density make it difficult to elaborate further.

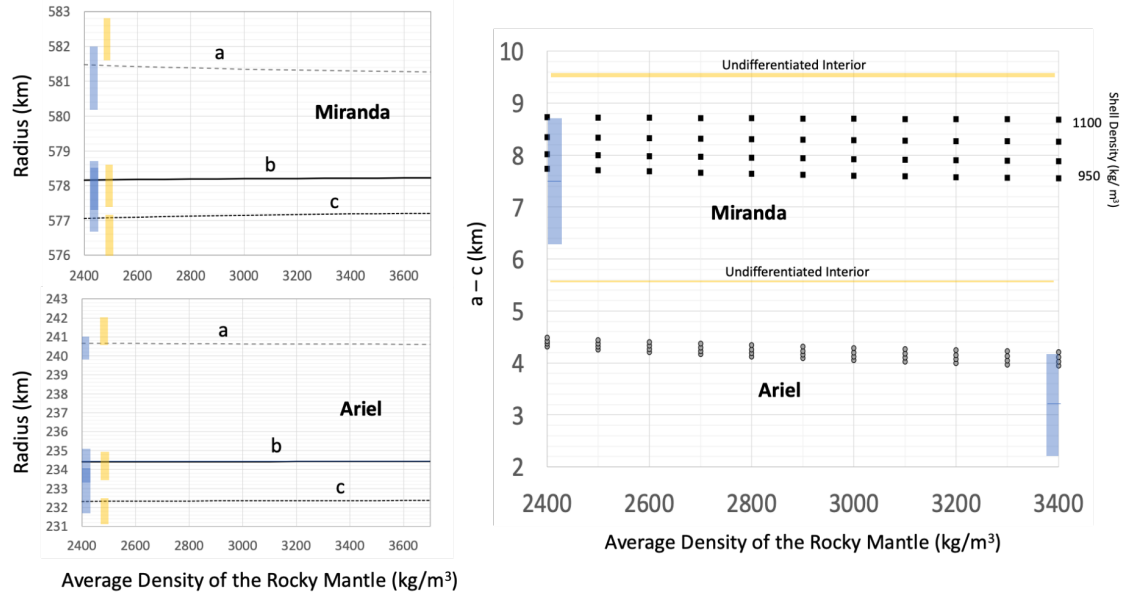


Figure 2. Evidence for differentiation of Ariel and Miranda from their shape. Left: Ellipsoidal axes ( $a$ ,  $b$ ,  $c$  radii) computed for two-layer (i.e., differentiated structure with rocky core and overlying ice-rich shell) models for Miranda and Ariel ( $\rho_{\text{shell}} = 1050 \text{ kg/m}^3$ ), compared against radii for undifferentiated interiors (yellow) and radii inferred from Voyager 2 observations reported in Archinal et al. (2018) (blue). Observed radii are presented with 1-sigma error bars. Right: Differences between  $a$  and  $c$  radii with the same color-coding but for four different shell densities.

In the case of Ariel, the mean value of the observed  $(a-c)$  is lower than the values predicted for a two-layer interior. The weak dependence of  $(a-c)$  on core density compared against the error bar again precludes further inferences on Ariel's evolution. Altogether, these observations suggest with high (2-sigma) confidence that the two moons underwent some level of differentiation.

In both cases, the ratio of  $(b-c)$  to  $(a-c)$  departs from the  $\frac{1}{4}$  value expected for a body in hydrostatic equilibrium (e.g., Zharkov et al. 1985). This suggests that the moons' shapes may depart from hydrostatic equilibrium, which limits the extent of interpretation of the radii reported in Archinal et al. (2018).

## 2.2 Surface Evolution from Geological Imaging



Analysis of crater densities for the Uranian moons Umbriel, Titania, and Oberon indicate that they could have largely ancient surfaces ( $\sim 3\text{--}4$  Ga, Zahnle et al. 2003) and, therefore, surface expressions of endogenic activity may be largely relegated to the geologic past on these moons. In contrast, crater densities indicate that Miranda and Ariel have younger surfaces in some regions. As summarized in Kirchoff et al. (2022), surface ages may be as young as 0.1 ( $-0.1/+0.4$ ) Ga for Inverness Corona on Miranda. The most recent estimates for Ariel’s surface age are 1.3 ( $-0.6/+2.0$ ) Ga with some tectonic features estimated to be as young as 0.8 ( $-0.5/+1.8$ ) Ga.

Thermal stresses are thought to be responsible for the older extensional tectonic features on the classical Uranian satellites, although some features have likely been erased from impact events (Hillier and Squyres, 1991). Expansion of the lithosphere during freezing of the interior may have also contributed to the formation of extensional faults on these satellites (Smith et al., 1986; Croft and Soderblom, 1991).

Miranda was previously hypothesized to have broken up and re-accreted (e.g., Janes and Melosh, 1988), which would have accelerated cooling. This re-accretion model was proposed to explain Miranda’s large deformed regions, termed coronae, under the assumption that the coronae formed by contraction due to subsidence of surface terrains. However, more recent work indicates that the coronae are likely extensional structures formed from uplift, possibly due to diapirism, in contradiction with the re-accretion model (e.g., Pappalardo et al., 1997; Hammond and Barr 2014). Diapirism, an expression of solid-state convection, would necessitate tidal heating because radiogenic heating alone is unable to produce sufficiently high temperature gradients and low ice viscosities after a few hundred million years (My).

The relatively high eccentricities observed at all the moons ( $\sim 0.1\%$  and up to  $0.3\%$  for Umbriel) indicate the average dissipation inside these moons has been small in recent time, which is reflected in the high  $Q/k_2$  values derived by Cuk et al. (2020) (gathered in Table 1), within the assumptions (in particular Uranus’  $Q/k_2$ ) used in that study. Hence, the moons current heat budget is limited to long-lived radioisotope decay (see Hussmann et al. 2006; Chen et al. 2014; Table 1) with production power scaled to surface area of the order of  $0.1\text{ mW/m}^2$  in the case of Miranda,  $\sim 0.7\text{ mW/m}^2$  for Ariel and Umbriel, and  $\sim 1\text{ mW/m}^2$  for Titania and Oberon.

The surfaces of Miranda and Ariel display evidence for geological activity more recent than 1 Ga (Zahnle et al. 2003). Detailed analysis of geological features have led to constraints on past surface heat flow. Assuming a lithosphere composed of pure water ice, Peterson et al. (2015) estimate Ariel’s heat flows range between  $29$  and  $92\text{ mW/m}^2$  (almost 1-2 orders of magnitude higher than current heat flows) for a region in the center of Ariel’s relatively old “Pixie Group” of chasmata (Peterson et al. 2015), while surrounding chasmata in this group exhibit lower heat flows ranging from  $6\text{--}36\text{ mW/m}^2$  (Beddingfield et al., 2022a) and those in the younger “Kachina Group” of chasmata range from  $17\text{--}46\text{ mW/m}^2$

(Beddingfield et al., 2022a).

Peterson et al. (2015) and Beddingfield et al. (2002a) interpret their heat flow estimates at Ariel as the result of an eccentricity resonance, likely the 5:3 MMR resonance with Umbriel. Peterson et al. suggest an eccentricity of 20 to 50 times the current value is needed in order to match the highest estimated heat flows. By comparison, Cuk et al. find a maximum eccentricity during the 5:3 MMR of  $\sim 0.01$ , or only about 10 times the current value. Hence, the range of heat flows derived by Peterson et al. and Beddingfield et al. corresponds to  $Q/k_2$  between 5 and 76.

In the case of Miranda, Beddingfield et al. (2015) inferred a heat flow of 31–112 mW/m<sup>2</sup> during the formation of Arden Corona, and Beddingfield et al. (2022b, under review) inferred a heat flow of 35–140 mW/m<sup>2</sup> during the formation of Inverness Corona. Cuk et al. (2020) showed that secular perturbations exerted by Ariel during the Ariel:Umbriel 5:3 MMR increased Miranda’s eccentricity, which could trigger significant tidal heating. Cuk et al. (2020) suggested that during this resonance, this level of dissipation could be reached if Miranda’s  $Q/k_2$  was  $10^2$ – $10^3$ .

### *2.3 Surface Composition*

Recent ground-based telescope observations of the Uranian moons detected carbon dioxide (CO<sub>2</sub>) ice (Grundy et al. 2003, 2006; Cartwright et al. 2015, 2022) and possibly ammonia (NH<sub>3</sub>) and ammonium (NH<sub>4</sub>)-bearing species (Bauer et al. 2002; Cartwright et al. 2018, 2020) on their surfaces.

The accretion of non-water volatiles in the Uranian system is expected, based on cosmochemical models (Kargel and Lunine 1998). In solution CO<sub>2</sub>, CO (carbon monoxide) and NH<sub>4</sub> should produce CO<sub>3</sub>-NH<sub>4</sub> rich liquids (Castillo-Rogez et al. accepted). Both Ceres and Enceladus display spectral evidence for carbonates. Cassini detected ammonia (NH<sub>3</sub>) in plume material jetting out of Enceladus (see Ray et al. 2021 for a review). Ceres has ammonium (NH<sub>4</sub>)-salts and clays across its surface (Raponi et al. 2019). Both species have been associated with the presence of a deep ocean, based on their association with geological features and ongoing exposure via volcanic activity. Ammonia ices or ammonium salts have also been found on Charon’s surface (see Protopapa et al. (2021) for a review).

Cartwright et al. (2020) suggested that the presence of NH<sub>3</sub> and NH<sub>4</sub>-minerals on the surfaces of the Uranian moons. Because NH<sub>3</sub>-bearing species exposed on the surfaces of these moons may be efficiently decomposed over geologically short timescales by charged particles (e.g., Moore et al., 2007), this could point to a replenishment mechanism involving a deep ocean. On the other hand, the spectral signature of NH<sub>3</sub> could persist over longer timescales if irradiated fragments are able to recombine or if they form ammonium (NH<sub>4</sub><sup>+</sup>) cations that interact with surrounding molecules to make NH<sub>4</sub>-rich salts that could be more resistant to charged particle weathering (Cruikshank et al., 2019).

In the case of the Uranian moons, we lack spatially resolved reflectance spectra collected over different regions and geologic units. Hence, the origin of these compounds, whether from the deep interiors of the Uranian moons or whether they are products of surface chemistry is not known. As a replenishment mechanism, subsurface  $\text{NH}_3$  might readily diffuse through the  $\text{H}_2\text{O}$  ice shell to the surface (Livingston et al. 2002). The rate of diffusion could be enhanced by craters and other landforms that increase fracturing and porosity (see discussion in Cartwright et al. 2020). A limitation is that  $\text{NH}_3$  diffusion rates at temperatures relevant to the Uranian moons are not well constrained.

### 3. Modeling Approach and Setup

Like previous studies (Hussmann et al. 2006; Bierson and Nimmo 2022), our thermal modeling assumes conductive heat transfer. A major difference is the coupling between thermal and geochemical modeling, which has important implications. For example, many studies of icy moon evolution have assumed that accreted ammonia remains entirely available as antifreeze, when in practice ammonia turns partly into ammonium once in aqueous solution (e.g., Marion et al. 2012). On the other hand, other solutes such as chlorides can significantly decrease the eutectic temperature. Models have also assumed the occurrence of clathrate hydrates as possible insulating material but, as shown later in this paper, this prospect is highly dependent on environmental conditions (e.g., Sloan and Koh 2008; Castillo-Rogez et al., accepted).

We assume the moons accreted in a circumplanetary disk (CPD), which determines a range of compositions for the material accreted in the moons. Alternative formation scenarios and their implications for thermal evolution are addressed in Section 5.1. After a general description of the thermal modeling approach, we describe the input parameters specific to these various features.

#### 3.1 Thermal Modeling Approach

Our internal evolution modeling assumes differentiation of a mostly lithified rocky core and hydrosphere (ocean and ice-rich shell) (e.g., Hussmann et al. 2006). We use the one-dimensional thermal conduction model described in Castillo-Rogez et al. (2007, 2019). Hussmann et al. (2006) suggested that objects in the size range and surface temperature of the Uranian moons are either not likely to convect or that convection played a minor role in their evolution. King et al. (2022) predict that convection was possible in these bodies, assuming a pure water ice composition. On the other hand, rock grain impurities could likely increase the effective viscosity of the crust and impede the onset of convection (e.g., Qi et al. 2018). Also, porosity can counteract the buoyancy of deeper layers by creating a negative density gradient with decreasing depth. Here we assume that the shells are not convecting, which leads to optimistic evolution outcomes in terms of liquid preservation.

The extent of early differentiation is primarily driven by the time of formation with respect to calcium aluminum-rich inclusions (CAIs), which determines the amount of accreted short-lived radioisotopes, in particular  $^{26}\text{Al}$ . Accretional

heating represents a small contribution to the heat budget in objects less than 1000 km in diameter (e.g., Matson et al. 2008) but it can help decrease the primordial microporosity in the crust as a result of compaction creep. Long-term internal evolution is driven by the heat from long-lived radioisotope decay and potentially tidal heating. At present, tidal heating does not represent a significant heat source but it could have been important during periods of resonances (see Section 2).

### *3.2 Reference Rock and Volatile Compositions*

Formation in the CPD reflects the solar nebula composition with potential addition of pebbles from farther out in the disk (e.g., Mousis et al. 2020). Although it has been suggested that Uranus migrated significantly during its growth, starting potentially at 7-10 AU or 9-15 AU in the protoplanetary disk (Thommes et al. 1999; Morbidelli and Nesvorný 2012; Helled and Bodenheimer 2014), the moons could have formed by the time the planet reached its current location (Szulágyi et al. 2018).

We assume a CI carbonaceous chondrite composition (Appendix A) with the addition of volatiles (Appendix A), which is likely appropriate for bodies formed at 10 to 19 AU (e.g., Desch et al. 2018; see Melwani Daswani and Castillo-Rogez 2022 for more detail). We explore two reference fractions of accreted  $\text{NH}_3$  of 0.3 and 1 wt.% and initial abundances of  $\text{CO}_2$  at 1 and 5 wt.%. Alternative moon origin scenarios and their implications for the moon evolution are discussed in Section 5.1. The geophysical implications of accreting pebbles formed farther out (e.g., Mousis et al. 2020) are discussed in Section 5.2.

### *3.3 Material Thermophysical Properties*

#### *3.3.1 Rock Phase*

Previous studies have assumed a rock density of  $3500 \text{ kg/m}^3$  (Bierson and Nimmo 2022) for the Uranian moons, but this assumption is not consistent with the expected state of the core following differentiation as rock hydration is a relatively fast process ( $\ll 1 \text{ My}$ , e.g., Martin and Fyfe 1970; Zandanel et al. 2022). As the prospect of preserving a deep ocean depends in part on the thickness of the overlaying shell, it is important to track the rock density evolution with temperature. Instead, we assume that during and following differentiation, the rock phase could become fully hydrated. This is supported by recent experimental work by Zandanel et al. (2022) who showed that aqueous alteration of rock in icy bodies proceeds on geologically fast timescales (a few My to tens My), even at low temperatures (at least as low as 250 K).

The starting density of hydrated CI chondrite refractory material prior to thermal metamorphism is about  $3060 \text{ kg/m}^3$  (at 273 K and 1 bar). This number results from thermodynamic equilibrium of all the phases in CI chondrites. The evolution of the rock density as a function of pressure and temperatures is mapped over the range of conditions relevant to the Uranian moons (Figure 3). This density is calculated with the Gibbs energy minimization program

Perple\_X (Connolly 2005; 2009) which computes the thermodynamically stable phase assemblage, including fluid composition (Connolly and Galvez 2018; Galvez et al. 2015). In the case of a 100% CI chondrite composition, the representative phase assemblage consists of talc + antigorite + siderite +  $\text{H}_2\text{O}$  + pyrite or troilite + chlorite + ankerite + graphite  $\pm$  magnetite  $\pm$  dolomite at low temperature (region **A** in Fig. 3). At moderately high temperatures (**B**), carbonates and antigorite are destabilized, yielding olivine +  $\text{H}_2\text{O}$  + amphibole + troilite +  $\text{CO}_2$  + chlorite + graphite. Finally, amphiboles are dehydrated at high temperatures (**C**), yielding olivine +  $\text{H}_2\text{O}$  + troilite + orthopyroxene +  $\text{CO}_2$  + anorthite + clinopyroxene + graphite.

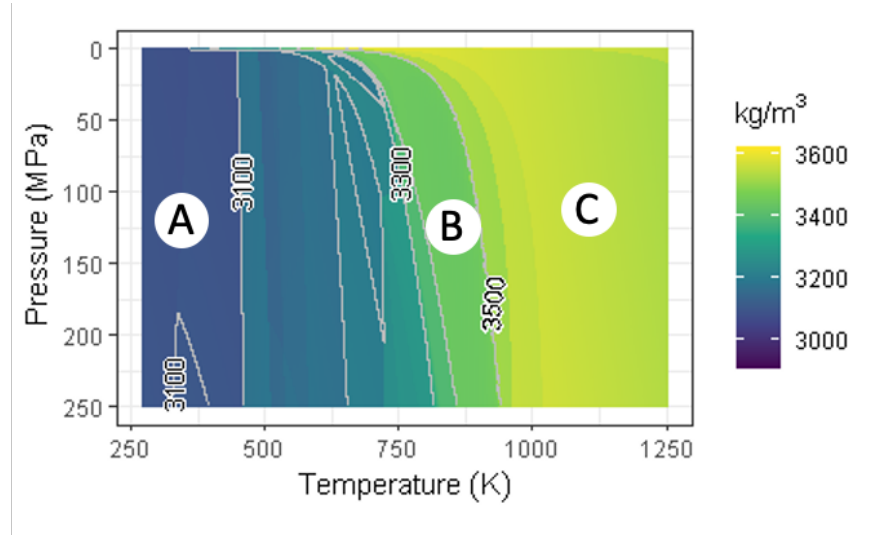


Figure 3. Density of the rock phase as a function of temperature and pressure for a CI chondrite composition [based on Palme et al. (2014)]. See Table A.1 for further details about the reference elemental composition. This chart covers the pressure and temperature domains relevant to the moons’ rocky cores.

In the pressure-temperature conditions expected in  $<1000$  km radius icy moons, insoluble organic matter (OM) is degraded into graphite at low temperature ( $<300$  K, Melwani Daswani and Castillo-Rogez 2022). The fate of graphite is not well understood. It could potentially migrate from the rock with fluids also released from thermal metamorphism, or it could remain trapped in the rocky cores. In the latter case, graphite’s high thermal conductivity, 10 to 20 times that of rock (e.g., Pavlov et al. 2017) could accelerate the cooling of the core. Soluble organic matter that sunk with rock during differentiation would also degrade under low-grade metamorphic conditions and release small-chain molecules to the ocean (Melwani Daswani and Castillo-Rogez 2022). The fraction of organic matter that would eventually remain in the core has not been modeled in detail but should be considered in future work. In the case of Ceres, Melwani Daswani and Castillo-Rogez (2022) found that the rocky interior

would contain 1 to 3 wt. % of carbon at the end of metamorphism, if Ceres has a carbonaceous chondrite composition.

Rock thermal conductivity ( $T_c$ ) shows little dependence on temperature above 300 K (e.g., Opeil et al. 2010, 2020). However, the  $T_c$  of dry rock can decrease to 1 W/m/K at 70 K. Opeil et al. (2010, 2020) showed that the  $T_c$  of CM chondrites is <1 W/m/K between 70-300 K. The  $T_c$  of ordinary chondrites (H and L) is ~1.5-2 W/m/K at and above 100 K. We also use specific heat capacities for carbonaceous materials reported in Opeil et al. (2020, Table 3).

### 3.3.2 Ices

The  $T_c$  of H<sub>2</sub>O ice at the effective surface temperature at 19 AU (~70 K) is about 7.5 W/m/K (e.g., Slack 1980). At 273 K, the water ice  $T_c$  is 2.3 W/m/K. Hence, the prospect for the Uranian moons to preserve a deep ocean despite their cold environment depends in part on the presence of porosity or of materials that act as insulators.

Porosity could be preserved in the crust, depending on its composition and thermal evolution. Bierson and Nimmo (2022) assume the preservation of porosity in a pure ice shell, assuming the body is already differentiated. However, Neumann et al. (2020) showed that bodies with a cold crust, such as Kuiper belt objects, may preserve a thick and undifferentiated crust. That is, a porous crust would also entail the presence of silicate and other compounds, such as non-water ices (e.g., NH<sub>3</sub> hydrates, and CO<sub>2</sub>). The effective thermal conductivity of a mixture of materials is the sum of the relative volume fractions of each material. Previous studies have assumed that the microporosity of freshly accreted material may be up to 50% (e.g., Eluszkiewicz and Leliwa-Kopystyński 1989). To account for the effect of porosity, we use the relationship derived by Bierson et al. (2016) based on the Shoshany et al. (2002) empirical results. This equation is valid for a porous mixture if the fraction of porosity  $\Phi_p$  = 0 to ~20%. For higher fractions the effect becomes more complex as grains may become loosely connected (e.g., Shoshany et al. 2002). For  $\Phi_p$  = 0.5, the thermal conductivity can be decreased by >50%.

The thermal conductivity of a mixture at 70 K with ~50 vol.% ice at 7.5 W/m/K and 50 vol.% rock at ~1 W/m/K is about 5.0 W/m/K.  $\Phi_p$  = 50% decreases this value below 1 W/m/K and  $\Phi_p$  = 20% to ~4.1 W/m/K. At 150 K, the  $T_c$  of the ice-rock mixture is ~3.1 W/m/K. If  $\Phi_p$  = 20% remains at the corresponding pressure, then  $T_c$  may be ~2.2 W/m/K. Our thermal modeling tracks the evolution of  $T_c$  with compaction, composition (porous mixture vs. ice and rock layers) and temperature. Lastly, the core size is adjusted based on the amount of rock trapped in the undifferentiated crust.

### 3.3.3 Conditions for Clathrate Formation

Depending on the composition of accreted volatiles and internal evolution, clathrate hydrate formation may be possible (see Castillo-Rogez et al., accepted; hereafter referred to as CR22). It depends primarily on the fate of

accreted carbon ices, in particular how much  $\text{CO}_2$  is dissolved into the ocean (which occurs when  $\text{pH} \ll 7$ ) and how much is turned into carbonates (which occurs when  $\text{pH} \gg 7$ ) (see CR22). For the several wt.% of  $\text{CO}_2$  and  $\sim 1$  wt.%  $\text{NH}_3$  expected in the Uranian moons (e.g., Mousis et al. 2020), the oceanic environment is more likely to be favorable to the formation of carbonates, resulting in a high fraction of bi/carbonate ions in solution (CR22).

We examined the freezing of the only scenario in CR22 that could lead to a  $\text{pH} < 7$  and the concentration of  $\text{CO}_2$ , which occurs when the accreted  $[\text{CO}_2] = 5$  wt.% and  $[\text{NH}_3] = 0.3$  wt.% and a water to rock ratio of 10 (we refer the reader to that paper for more context). The molality of  $\text{CO}_2$  at equilibrium is 0.3 mol/kg. FREZCHEM modeling shows that water is still primarily used for ice formation and only 1.5 mol.% of water is used for the formation of clathrates, leading to the production of a marginal amount of that material. Clathrate formation consumes residual liquid until full freezing at about 250 K. The thickness of a global layer of  $\text{CO}_2$  clathrates formed in this example is 7 km and lies below a  $\sim 220$  km thick ice shell. However, the production of clathrates could be inhibited by the presence of salts (e.g., Sloan and Koh, 2008), although this inhibition might be counteracted by a self-preservation mechanism for low salt concentrations ( $< 0.2$  mol; see Boström et al., 2020). For a high salt concentration in a residual ocean, clathrates are likely to become unstable, resulting in erosion of clathrate accreted in the shell and the release of  $\text{CO}_2$  in the residual ocean. Although a more extensive survey of the chemical environments of Uranus' moons falls outside the scope of this work, it appears that the occurrence of clathrates is unlikely. Hence, we did not include them in our models.

CR22 also show that the fate of the  $\text{CO}_2$  is in part determined by the effective water-to-rock ratio, W/R (i.e., the mass of water that a unit mass of rock is exposed to during aqueous alteration). This parameter is not well constrained but the literature on icy moons and carbonaceous chondrite parent bodies has reported W/R values of the order of 0.5-4 (see CR22 for a review). Hence we take an  $\text{W/R} = 1$  as a reference for this study. In these conditions, the bulk of  $\text{CO}_2$  is primarily consumed in the production of carbonate salts and carbonate ions and little  $\text{CO}_2$  concentrates in solution.

As a result, the formation of  $\text{CO}_2$  clathrates is unlikely in this kind of system (see Section 5.2 for additional discussion). Methane clathrates are not expected either, because there is little methane in the system. Kamata et al. (2019) and Carnallan et al. (2022) have suggested methane clathrates to be abundant in large icy bodies due to the breakdown of abundant organic matter mixed with rock in the core of these bodies. In the case of Ceres, a relevant analog to the Uranian moons in terms of size (central pressure  $\sim 150$  MPa), radioisotope heat budget, and composition, Melwani Daswani and Castillo-Rogez (2022) show that the output of methane from thermal metamorphism of the core is negligible.

### *3.4 Heating from Radioisotope Decay*

We include heat produced from the decay of short- ( $^{26}\text{Al}$ ) and long-lived (uranium U, thorium Th, and potassium K) radioisotopes. For an origin in Uranus' CPD, we assume a time of formation between 3 and 4.5 million years (Ma) after CAI-formation, consistent with aforementioned references (Section 3.2). We use the CI composition for K, U, and Th abundances (e.g., Lodders 2021) (see Appendix B).

The potential extraction of K as a consequence of rock-leaching during a phase of aqueous alteration and the potential exchange of  $\text{NH}_4^+$  with  $\text{K}^+$  (Engel et al. 1994; Zolotov and Shock 2001; Neveu et al. 2017) are possibilities depending on the moon and its aqueous environment. From modeling the dependence of ocean composition on various parameters, in particular the effective W/R, CR22 found that the fraction of K leached from the rock may range from 10 to 30% of the accreted K abundance. For the W/R  $\sim 1$  assumed for the small moons considered in this study, K leaching is limited (about 10%). Melwani Daswani and Castillo-Rogez (2022) find that up to 50% of the K may be redistributed from the processed rock to the liquid phase as a consequence of thermal metamorphism. This displacement of a major heat source could contribute to heating the base of the hydrosphere (see Castillo-Rogez et al. 2019). However, we show below that thermal metamorphism was generally limited in extent in the Uranian moons, except maybe for Titania and Oberon.

### 3.5 Heating from Tidal Dissipation Post-Resonance

The tidal heating rate depends on a moon's orbital properties as well as its internal properties expressed in the form of the tidal Love number,  $k_2$ , and dissipation factor,  $Q$ . Both parameters are dependent on the tidal forcing frequency,  $n = 2/P$ , where  $P$  is the orbital period. The heating rate, time-averaged over the spin-synchronous body's orbit and averaged over its interior under the assumption of a small eccentricity and zero obliquity, can be estimated as  $W = k_2/Q \cdot 7e^2 (3/2 G M_U^2 n R^5 / D^6)$  (e.g., Renaud et al., 2021), where  $G$  is the gravitational constant,  $M_U$  is the mass of Uranus, and other parameters are given in Table 1. It is important to note that all other things being equal, tidal heat production in the Uranian moons would be  $\sim 50$  times less than in the Saturnian moons due to Uranus' lower mass.

Because of the moons' limited long-lived radioisotope budget, dramatic geological events may reflect increased tidal heating via resonance crossings. As discussed in section 2.2, the most recent one is thought to be the Ariel:Umbriel 5:3 MMR, which Cuk et al. (2020) have shown to influence the moon system on a global scale. Cuk et al. (2020) modeled the evolution of the moons' orbital properties since they broke from their latest resonances (Table 1). We are not considering these events as part of our thermal evolution modeling because they require combining dynamical and thermal evolution, which is beyond the scope of this work. Outside dynamical resonances, the heating rate from the dissipation of solid tides is several orders of magnitude lower than that from radioisotope decay, depending on the moon (see also Chen et al. 2014).



We added to Table 1 the estimated power generated from obliquity-driven tides in the moon oceans (assuming they hold large oceans at present) following Chen et al. (2014). This power source contributes at most a few MW in the case of Miranda and Oberon. Altogether, the combined energy produced by present-day tidal dissipation is several orders of magnitude less than the integrated energy lost via conduction through the ice shell in the case of Miranda ( $\sim 0.002$  GJ/s produced versus 0.3 GJ/s lost for an average crustal  $T_c$  of 1 W/m/K).

We compute the tidal Love number and dissipation factor in order to compare the current state derived from our thermal models to the Cuk et al. (2020) estimates. These parameters are computed for multilayered interior models for the moons derived from the thermal evolution models. We use the modeling approach described in Castillo-Rogez et al. (2011) in which the material response to tidal forcing accounts for anelasticity via the Andrade rheology model (Andrade 1910) fit by laboratory measurements. The Andrade model includes an anelastic component represented by an infinite number of dashpots in series in parallel with an infinite number of springs and represents a continuous distribution of compliances and thus relaxation times.

Because of the many uncertainties in the description of water ice’s viscoelastic behavior, we do not explicitly vary temperatures and grain size but instead consider a range of relevant viscosities between  $\sim 10^{14}$  Pa s (relevant for the water melting point) and  $\sim 10^{27}$  Pa s (relevant for  $< 120$  K). The viscoelastic properties of clathrate hydrates at the cold shell temperatures obtained in our models are unknown. Hence, the viscosities derived from the inversion of available  $Q/k_2$  estimates do not provide direct constraints on the shell composition. Results are presented in Sections 5.3 and 5.4.

### 3.6 Ocean Composition

We model the composition of the ocean as a consequence of freezing using FREZCHEM (Marion et al. 2010) based on earlier work (Castillo-Rogez et al. 2018). The fractions of  $[\text{CO}_2] = 1$  to 5 wt.% and  $[\text{NH}_3] = 0.3$  to 1 wt.% assumed in this study are on the low end of abundances predicted in the literature (see Hussmann et al. 2006) and thus provides a lower bound on the influence of that compound on the persistence of liquid in the large Uranian moons. A more extensive analysis of the parameter space is left for future work. The assumed

FREZCHEM produces the composition of precipitated solids (e.g., ice, gas hydrates, and salts) and residual liquid as a function of temperature and pressure. Liquid can remain at low temperature due to the presence of ammonia (peritectic at  $\sim 176$  K) and chlorides (eutectic at  $\sim 220$  K) in particular.

### 3.7 Electrical Conductivity

Our geochemical modeling approach uses the electrical conductivity (EC) estimates from CR22 following the general empirical model embedded in the Geochemist’s Workbench software (McCleskey et al. 2012). However, the applicability of that model is limited to dilute solutions [ $< 1$  mol/(kg  $\text{H}_2\text{O}$ )] and

experimental data for more concentrated solutions are missing. CR22 show that  $[\text{CO}_2] \sim 4 \text{ wt.}\%$  and  $[\text{NH}_3] \sim 0.3 \text{ wt.}\%$  leads to a salinity  $>1 \text{ wt.}\%$  prior to any freezing. For a solution dominated by  $\text{Na}^+$ ,  $\text{HCO}_3^-$ ,  $\text{NH}_4^+$ ,  $\text{Cl}^-$ , and  $\text{CO}_3^{2-}$ , this corresponds to an EC of about 1.5 S/m at  $0^\circ\text{C}$  and 1 bar (McCleskey et al. 2012).

As shown below, our thermal models yield thin oceans with high salt concentrations. For example, in a residual layer about 30 km thick, we find that the solution has a  $\text{Na}^+$  and  $\text{Cl}^-$  salinity of 150 g/kg of water ( $\sim 2.5 \text{ mol/kg}$ ) for a starting salinity (i.e., prior to concentration) of 1.5 wt.%. There is no general formalism for describing the EC of hypersaline solutions. For high ionic strength (above 1 mol/kg), the McCleskey et al. method is not applicable. Instead, we rely on analogs and laboratory studies to constrain the EC of hypersaline solutions. Direct measurements of NaCl brine at 273 K for a concentration of 149 g/kg yield an EC of 10 S/m (Oldenborger 2021). NaCl reaches saturation at about 357 g/kg (or  $\sim 6 \text{ mol/kg}$ ) at  $0^\circ\text{C}$ . Extrapolation of the temperature dependence of NaCl solubility suggests only a slight increase of this value at subzero temperatures (e.g., about 10% increase from 273 to 233 K; Cong et al. 2019). Brines saturated in sodium chloride are common on Earth and have conductivities of about 23 S/m for a reference temperature of 298 K (e.g., Rebello et al. 2020).

However, aqueous solution ECs show a positive dependence on temperature (e.g., Smith 1962; Pan et al. 2021). Hence, we use a temperature correction factor  $f_c$  (e.g., Smith 1962) to derive the EC at a targeted temperature  $T_0$ ,  $T_0$ , from the EC measured at a reference temperature  $T_{\text{ref}}$ ,  $T_{\text{ref}}$ :

$$T_0 = T_{\text{ref}} [1 + f_c (T_0 - T_{\text{ref}})] \quad [\text{E1}]$$

Correction factors found in the literature are largely consistent with each other and are of the order of 0.02/K (Smith 1962; Oldenborger 2021), independent of the composition. Hence, an EC of 23 S/m at 298 K scales down to an EC of  $\sim 12 \text{ S/m}$  at 273 K. Although in reality the correction factor depends on concentration and varies with respect to temperature and concentration (e.g., Oldenborger 2021), considering the many uncertainties in the composition of the ocean, we consider it a constant here ( $f_c = -0.02/\text{K}$ ).

#### *Brine-Filled Porous Core Models*

In the case of a porous core (e.g., that of Enceladus), the brine temperature may be above 373 K. In that case, the EC of a chloride-rich brine may be at least 50 S/m and potentially greater than 100 S/m (Ucok et al. 1980; Ussher et al. 2000). The EC of a mixture of this brine and the surrounding rock is computed with Archie's law. It defines the resistivity formation factor

$$F = \rho_0 / \rho_w$$

where  $\rho_0$  is the macroscopic resistivity (porous rock and brines) and  $\rho_w$  the resistivity of the pore fluid. Experimental work by Archie (1942) led to the inference that  $F$  is proportional to the porosity  $\Phi$  to an exponent  $m$  called the

cementation index:  $F = \Phi^{-m}$ . The value of the cementation index depends on the pore shape and the tortuosity. In an ideal situation where the flow of brines in the rock is unhindered,  $m$  tends toward 1. Values are generally found between 1.5 and 2.5 (Glover et al. 1997; Revil et al. 1998) and are about 2 for porous clays (Revil et al. 1998).

#### *Effect of Pressure*

Pressure tends to increase EC by up to ~10% at the pressures of tens of MPa that are relevant to the residual oceans considered in the Uranian moons (Horne and Frysinger 1963; Bradshaw and Schleicher 1980; Schmidt and Manning 2017; Pan et al. 2021). However, we lack measurements specific to the carbonate-rich compositions considered here. Overall, this effect is small because the pressures at the base of the moon shells are of the order of 40 to 70 MPa.

#### *Effect of Organics*

Some soluble organics can be charged and contribute to the EC, like for example carboxylic acids (CR2022). However, the abundance of these organics in solution is unknown. A 0.5 wt.% concentration of the carboxylic acid  $\text{CH}_3\text{COOH}$  yields an EC of 0.03 S/m while the acetate form  $\text{Na}^+\text{CH}_3\text{COO}^-$  expressed in alkaline conditions is 0.39 S/m (at 25°C). This could prove important for bodies whose residual oceans concentrate organic compounds (e.g., Ceres; Melwani Daswani et al. 2022).

### **4. Results of Thermal Modeling**

We describe the results obtained for the moons’ current thermal state (4.1) and prospect for the preservation of liquid at present (4.2). Examples of thermal evolution results are presented for Miranda, Ariel (which is also representative for Umbriel because the two bodies share similar physical properties), and Titania (which is also representative of Oberon) in Figures 4 and 5. First, we describe the findings of the thermal model. Then we assess the properties of the oceans that may be present in some of the moons at present. Possible evolutionary pathways are summarized in Section 4.4. As an important note of caution, many uncertainties in the history of these bodies and material properties allow only bounds on possible outcomes.

#### **4.1 Extent of Internal Evolution**

For bodies accreted in the CPD, presumably as a mixture of ices, rock, and porosity, differentiation of an ice-dominated shell and rocky core is not expected for all models. This end state requires sufficient heating to melt the ice phase on a global scale. This is realized for times of formation  $t_{0-\text{CAIs}} < 4$  My after CAIs for most of the moons (Figure 4). For  $t_{0-\text{CAIs}} > 4$  Ma, melting is partial and a thick porous, undifferentiated crust may overlay a solid icy mantle until present, of the order of 60 km in the case of Ariel and ~80 km for Titania (Figure 5). With a density of about 1000-1050 kg/m<sup>3</sup>, these crusts are unlikely to founder, consistent with the Neumann et al. (2020) study of Kuiper belt objects.

Due to its lesser rock content, Miranda would have to form  $<3$  My after CAIs, in order to differentiate a rocky core early on, which may not be consistent with the formation timeframe for the Uranian regular moon system. For later  $t_{0-CAIs}$ , our models indicate partial or no melting of Miranda’s ice and preservation of a large porosity fraction. If Miranda has differentiated a rocky core, as suggested by observations reported in Section 2, then it is likely the result of tidal heating, potentially during the event that formed Arden Corona (Beddingfield, 2015) and the thin lithosphere in that location (Pappalardo et al., 1997).

An additional event of differentiation may occur in some of the moons as a consequence of thermal metamorphism. In Titania and Oberon, part of the rocky core could reach the dehydration temperature of serpentine, at about 725 K, if the moons formed less than 5 My after CAIs and no K was leached from the rock early on. This would increase the density of the rock to above  $3100 \text{ kg/m}^3$  and lead to a late release of liquid to the hydrosphere (see Section 4.2). In the case of Titania, Figure B.1 shows the possible range of timing for metamorphism onset and fraction of impacted core as a function of the time of formation and other parameters. In the most favorable conditions (time of formation of 3 My after CAIs and no loss of K to the liquid phase during differentiation), up to 50 vol.% of Titania’s core could be dehydrated in the first 2 Gy after formation. A late ( $> 4$  Gy) stage of rock dehydration is possible but would affect only the central 10 vol.% of the core. Whether that liquid could reach the base of the hydrosphere or would react again (e.g., rehydration) with the ambient material is uncertain. Some thermal metamorphism is also predicted in Ariel and Umbriel if their core conductivity is lower than  $2 \text{ W/m/K}$ , but that process is limited to a radius  $<150$  km and thus the late release of liquid is minimal, assuming it could even upwell to the base of the hydrosphere.

Lastly, we find that the pressure and temperature conditions for differentiation of a metallic core are not met for any of the conditions explored in this study, which is consistent with Hussmann et al. (2006).

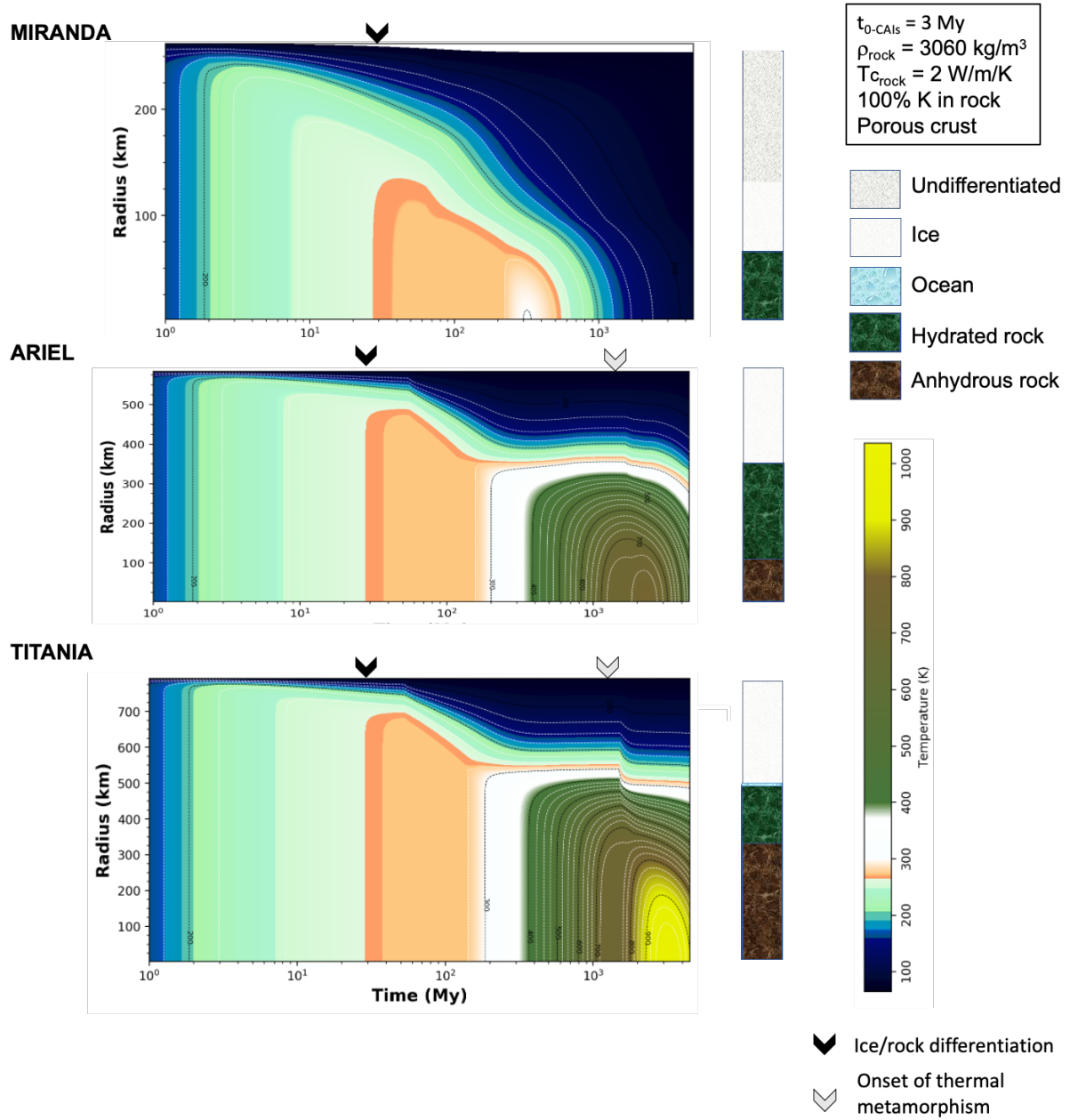


Figure 4. Examples of thermal evolution models for Miranda, Ariel, and Titania. Models assume a CI composition, a time of formation of 3 My after CAIs, and a starting porosity of 40%. Miranda's interior mostly compacts but partially melts and differentiates. On the other hand, Ariel and Titania undergo near global melting of their volatile phase (assuming foundering of a thin undifferen-

tiated shell) and differentiate a rocky core. The rocky core may undergo further differentiation as a consequence of thermal metamorphism in the case of Titania. The final interior structures outlined on the right assume current residual liquid is at the water freezing point. The Ariel and Titania thermal models are also representative of Umbriel and Oberon, respectively.

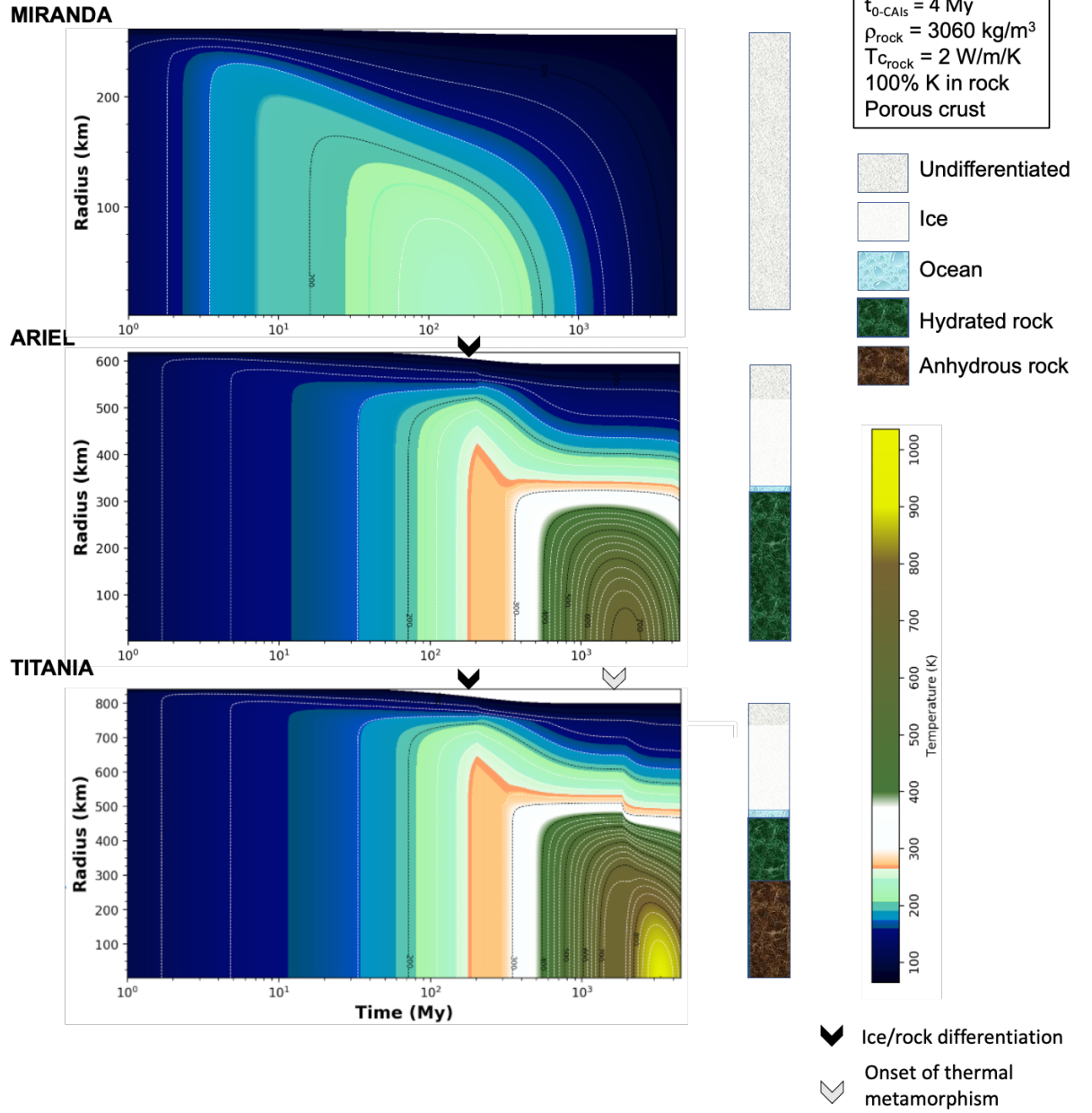
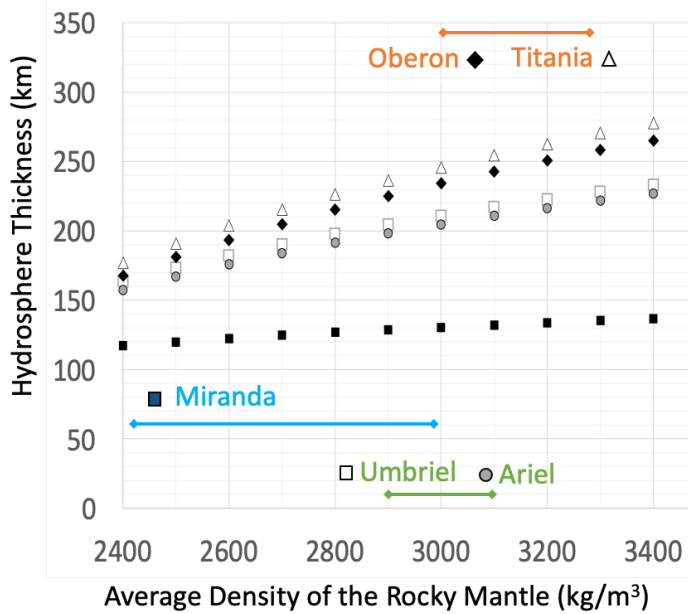


Figure 5. Same as Figure 4 for a time of formation of 4 My after CAIs. Miranda’s interior could not get warm enough for its interior to evolve, whereas Ariel’s and Titania’s ice could partially melt, leading to partial differentiation. The preservation of a porous lid on the latter moons enables the preservation of a  $\sim 10\text{-}20$  km liquid layer until present. Here, we represented the final interior structure assuming the water freezing temperature.

The range of hydrosphere thicknesses over the space of possible rocky core densities is represented in Figure 6 for all the moons, assuming the mean values for the radii and densities in Table 1. The hydrosphere thicknesses are  $\sim 200\text{-}220$  km in the case of Ariel and Umbriel and  $\sim 240$  to  $\sim 270$  km in the case of Titania and Oberon.

The bars map the more likely rock densities based on thermal modeling (the higher the peak temperature reached, the more devolatilized the rock and the higher its density; see Fig. 2). We note that the core temperature expected for Titania and Oberon corresponds to core densities of less than  $3200 \text{ kg/m}^3$ . This result differs from Bierson and Nimmo (2022) who assumed a rock density of  $3500 \text{ kg/m}^3$ , a dry rock value (similar to Io’s mean value) that does not appear consistent with the origin and evolution of the moons’ material.

Figure 6. Interior structures of the large Uranian moons. Models assume a two-layer interior, the mean bulk density values available in NASA’s Solar System Dynamics website, and a mean hydrosphere density of  $1000 \text{ kg/m}^3$ . The colored bars indicate the expected average densities for the rocky core based on thermal evolution modeling and the prospect for partial thermal metamorphism. A rock density greater than  $3400 \text{ kg/m}^3$  is not expected in any of the moons.



Considering Miranda’s small size, it is possible that the rock particles did not settle and form a compact core. Instead, the core could preserve  $\Phi_p = 20\text{-}30\%$  as modeled in the case of carbonaceous chondrite parent bodies in the same size range (Bland and Travis 2017) and per analogy with Enceladus (Neveu and Rhoden 2019). However, a high porosity core is unlikely in the other moons. The overburden pressure at the center Titania ( $\sim 240$  MPa) is one order of magnitude higher than at Enceladus. Compaction observations in pelagic environments show a drop in porosity from  $\Phi_p \sim 50\%$  to  $<20\%$  when the overburden pressure increases to 25 MPa. The porosity tends toward  $\Phi_p \sim 10\%$  at pressures  $> 150$  MPa (e.g., Allen and Allen 2005; Kim et al. 2018). At these porosities, permeability is very low, of the order of  $10^{-20}$  m<sup>2</sup> (e.g., Daigle and Screaton 2015). This is at least five orders of magnitude less than the permeabilities considered by Choblet et al. (2017) in their modeling of hydrothermal circulation in Enceladus’ core. In pelagic sediments, lithification starts at a lithostatic pressure of about 40 MPa, helped by cementation due to salt precipitation (e.g., Obradors-Prats et al. 2019; Neveu et al. 2015). The pressure at the base of Titania’s ice-rich shell is at least 65 MPa. Hence, it is very unlikely that the core of Titania would contain significant porosity. Following compaction and cementation, hydrothermal circulation that could control the temperature in the core (e.g., Choblet et al. 2017) shuts down and conductive heat transfer takes over, driving compaction creep (Neumann et al. 2019). A similar assessment applies to Ariel ( $\sim 45$  MPa at the base of the shell).

Neumann et al. (2019) and references therein show that Enceladus’ core is likely stratified as a result of this compaction-diagenesis-heating process, with a porous outer layer less than 10 km thick over a compacted inner core. In the case of Ceres, a bigger and denser body, Melwani Daswani and Castillo-Rogez (2022) show that Ceres’ low core density could be attributed to porosity introduced as a consequence of the release of brines following dehydration. A similar situation could happen in Titania and Oberon, but the modeling of this process is left for future work (see also Section 5.2).

## 4.2 Long-Term Preservation of a Deep Ocean

For a time of formation about 3 My after that of CAIs ( $t_{0\text{-CAIs}}$ ), short-lived radiogenic heating is high enough for Miranda’s internal temperatures to reach the water melting point and for some ice-rock differentiation to occur. However, the modeled interior entirely freezes by about 0.5 Gy after formation. Miranda is so small that outside of tidal resonances, it takes just a few tens of My for an ocean to freeze. Hence, the presence of a deep ocean in Miranda would imply that the moon was recently involved in some resonance. The rest of this section focuses on the larger moons.

Melting on a global scale leads to internal differentiation but also alters the properties of the shell via removal of porosity and second-phase impurities, such as ammonia hydrates, that would otherwise act in decreasing the shell thermal conductivity. As noted above, the formation of clathrate is not favored as CO<sub>2</sub> preferentially forms carbonates in the high-pH ( $>9$ ) environment fostered by



the presence of  $\text{NH}_3$ . Crustal porosity may be introduced later on by impacts, in the form of macroporosity, and potentially microporosity in a megaregolith built from ejecta.

The shell thermal conductivity is the primary property determining the long-term preservation of a deep ocean; liquid above the water eutectic can remain if the averaged shell thermal conductivity is less than 3 W/m/K (averaged). This is about a factor 2.5 lower than the value expected for a shell made of pure solid (non-porous) ice. This low  $T_c$  can be realized for a time of formation  $t_{0\text{-CAIs}} > 4$  My, leading to the retention of a thick porous layer on all the moons characterized (see Section 3). The second key parameter driving long-term liquid preservation is the amount of heat coming out of the rocky mantle, which is a combination of the rock thermal conductivity, 2 W/m/K, and the amount of potassium removed from the rock as a consequence of leaching.

#### *Additional Physical Processes Not Modeled*

Two events may help increase the prospect of a deep ocean at present: enhanced tidal heating through resonance crossing and a late phase of thermal metamorphism. Large-scale ice melting due to tidal heating would result in removing porosity. In these conditions, a transient ocean in Ariel formed 1 Gy ago may cool to below the water eutectic in a few tens of My and below 250 K in ~220 My. In the case of Titania, a tidally-generated ocean would cool below the water eutectic in about 250 My and contribute little to increasing the fraction of liquid preserved at present. An important implication of this short freezing timescale is that the present occurrence of brines is disconnected from occurrence of tidal heating events in the past. The four large moons may end up with similar thin residual oceans at present even if Ariel and Umbriel were subject to strong tidal heating in the past.

The release of fluids from the rocky core as a result of thermal metamorphism could theoretically supply additional amount of liquid equivalent to a 10 km thick layer in the case of Titania and Oberon and 2-3 km in the case of Ariel and Umbriel but the transfer of that liquid from the core to the hydrosphere is not handled in our models.

#### *Role of Composition*

The concentrations of key ocean compounds for three examples of non-water ice compositions are presented in Figure 7. This figure shows the drastic increase in  $[\text{NH}_3]$  in residual liquid layers less than 20 km thick, whereas  $\text{NH}_3$  and  $\text{NH}_4^+$  have about the same concentrations for thicker layers. Similarly, the concentration in  $\text{HCO}_3^-$  dominates over  $\text{CO}_3^{2-}$  in liquid layers a few tens of kilometers thick. The concentration of  $\text{Cl}^-$  steadily increases in a thinning ocean. As a result, the ocean density increases with its decreasing thickness up to 1040-1060  $\text{kg/m}^3$ , then decreases as ammonium bicarbonate ( $\text{NH}_4\text{HCO}_3$ ) precipitates; this leads to residual liquid enriched in ammonia, whose density tends toward 0.980  $\text{kg/m}^3$ . Sulfates are not produced in these conditions as sulfur is preferentially in the form of sulfides (see CR22).

For the fractions of 0.3-1 wt.% of  $\text{NH}_3$  accreted in our models, the residual ocean thickness at 180 K may be between 1 and 5 km (for a reference hydrosphere thickness of 220 km; see Figure 6). An ocean thickness up to 80 km has been suggested for Titania assuming accretion of 3 wt.%  $\text{NH}_3$  (Bierson and Nimmo 2022). Although this concentration is theoretically possible (e.g., Mousis et al. 2002),  $\text{NH}_3$  speciates into  $\text{NH}_4^+$ , which is then removed from the system in the form of precipitated salts ( $\text{NH}_4\text{Cl}$  and  $\text{NH}_4\text{HCO}_3$ ) at temperatures below  $\sim 250$  K. Depending on the ocean conditions, the residual fraction of  $\text{NH}_3$  may be only  $\sim 10\%$  to  $50\%$  of the accreted amount.

Oceans at a temperature greater than 245 K are of greater interest in this study because the ocean EC starts increasing with temperature and also because the habitability potential of these oceans becomes of interest (e.g., Clarke 2014). Chlorides can also play an antifreeze role and preserve residual liquid layers above 245 K. The thickness of these layers is still just a few to  $\sim 10$  km.

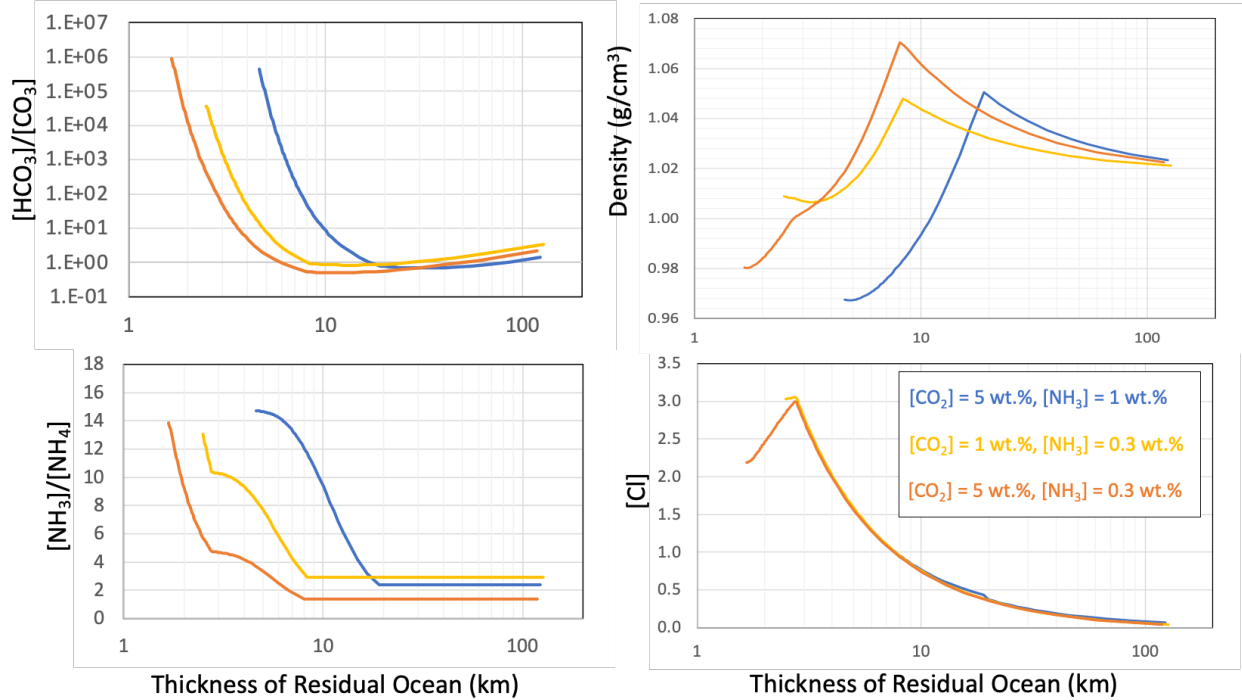


Figure 7. Some characteristics of residual liquid layers evolving from a thick ocean. Concentrations are in mol/kg. The ocean thickness is computed for Ariel assuming a 220 km initial ocean layer. The results are scalable to Titania and Oberon.

#### 4.4 Summary

We summarize the possible outcomes for the five moons (Figure 8).

### *Miranda*

Early differentiation in Miranda is unlikely but significant tidal heating during resonance crossing could have triggered extensive melting and late differentiation of a rocky core, which could explain available shape observations (Section 2.1). However, the probability for liquid to be preserved at present is nil, unless unknown dynamical circumstances are at play.

### *Ariel*

The thermal evolution of Ariel is in large part determined by its time of formation. For  $t_{0-CAIs} < 4$  My,  $^{26}\text{Al}$  decay heating was sufficient to trigger global melting, differentiation of a hydrated rocky core, and porosity closure. A later time of formation leads to partial interior melting and differentiation and the preservation of an undifferentiated porous crust tens of kilometers thick. In both cases, intense tidal heating during resonance crossing could result in at least partial melting of the volatile phase. Resurfacing observed on a near global scale likely involved the closure of crustal porosity, as suggested by the high heat flow recorded in the geology. As a result, resonance crossing could “reset” the structure of the hydrosphere. After breaking from resonance, crustal insulation would have been limited so that the preservation of liquid above the water freezing point is unlikely. A late release of fluids as a consequence of thermal metamorphism was possible but limited in extent.

### *Umbriel*

Umbriel’s evolution is similar to Ariel, except for more limited tidal heating and no significant implications from resonance crossings, as suggested by its older surface. As a result, the long-term retention of porosity could help preserve ~10-15 km of liquid until present.

### *Titania and Oberon*

Like Ariel and Umbriel, formation in  $<4$  My after CAIs would lead to global melting and differentiation of a rocky core. About 10 km of liquid above the water freezing point could remain at present, with potentially a late contribution of fluids evolved from core metamorphism (up to 10 km). For a later time of formation, up to 80 km of undifferentiated, porous crust could be retained, helping preserve up to 30 km of liquid.

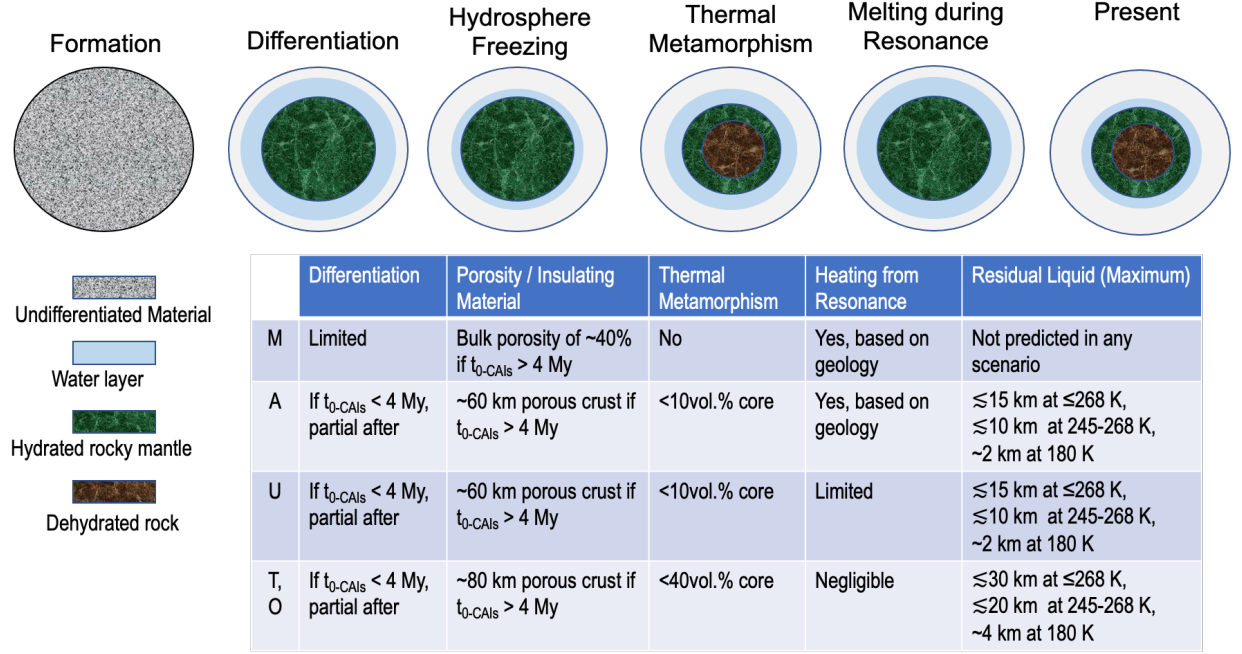


Figure 8. Stages of evolution and projected outcomes for the Uranian moons and prospects for liquid preservation in these bodies. Significant porosity may remain if the bodies formed later than 4 My after CAIs and act as insulator. For Miranda and Ariel, porosity would likely be removed during intense heating generated during resonance crossing. We distinguish residual oceans at a temperature greater than the water freezing point (268 K when accounting for pressure); (2) residual liquid at a temperature of 245 K where the electrical conductivity is significant, and (3) colder oceans kept liquid due to the presence of ammonia but which have near-zero conductivity.

## 5. Discussion

### 5.1 Assumptions on Origin and Composition

There are three formation models for the satellites presented in the literature: formation in the CPD, formation from a ring of ejecta from the giant planets, and late formation within a ring-moon system.

A formation in the CPD is most likely to allow accretion of carbon-based ices (Mousis et al. 2020). The most recent CPD model suggests that the moons formed toward the end of the CPD lifetime (Szulágyi et al. 2018). Except in the case of Miranda, if the moons formed less than about 3.5 My after CAIs, then they would be able to fully differentiate an ice-enriched shell from a rocky interior. For longer times of formation, Titania and Oberon would keep a thick porous and undifferentiated crust that would help preserve deep liquid until present. This reinforces the prospect that Titania and Oberon are likely to host

deep oceans at present.

Pebbles of cometary origin might enrich the volatile budget of the moons (Lambrechts et al. 2014; Helled et al. 2020). The addition of pebble material of cometary composition decreases the bulk content in radioisotopes. In particular, elemental measurements at 67P by the Rosetta mission (Table A.1) report a factor five depletion in aluminum and factor three depletion in iron with respect to a CI composition (see references in Appendix A). Potassium appears to be depleted by a factor 2. Data for U and Th are missing but the abundances of these refractory elements are also expected to be lower than in CI material. On the other hand, a cometary component increases the carbon and nitrogen fraction of the mixture in the form of additional organic matter and volatiles such as  $\text{CO}_2$  and  $\text{NH}_3$ . It was recently proposed that a large fraction of organics matter, up to 40 vol.%, could be responsible for the relatively low rocky mantle densities inferred for Titan and Ganymede (Neri et al. 2019). However, these models have not accounted for the thermal implications of organic matter’s low thermal conductivity, up to one order of magnitude lower than rock’s thermal conductivity (e.g., Zhu et al. 2019; He et al. 2021). As noted in Section 3.3, organic matter is likely to be converted to thermally conductive graphite at low temperature ( $<400$  K) and/or break down into smaller molecules at higher temperatures ( $\sim 550$  K) (see Melwani Daswani and Castillo-Rogez 2002, Figure 5). These temperatures are expected in Ariel, Umbriel, Titania, and Oberon (see Figures 4, 5). Hence, the viability of models with large fractions of organic matter remains to be demonstrated.

Another formation model for Uranus’ regular moons is that they accreted from ejecta after Uranus encountered a large impactor that could also be responsible for its obliquity (Morbidelli et al. 2012; Salmon and Canup 2022). Two important implications of this model are that (a) the moon material could contain a significant fraction of impactor material (Kegerreis et al. 2018); (b) also, Ida et al. (2020) predict that the temperature in the disk formed from ejecta could be  $>1000$  K and lead to a significant loss of water. We infer that more volatile species, like  $\text{NH}_3$  and  $\text{CO}_2$ , could also be lost in the process, although this needs to be considered in greater detail. In these conditions, the moons’ non-ice volatiles might be depleted in comparison to a formation in the CPD.

Lastly, a ring origin for the moons suggested by Crida and Charnoz (2012) based on a similar scenario proposed for Saturn’s moons (Charnoz et al. 2011) may have different long-term outcomes depending on the composition of the rings. In this model, the moons would form from the accretion of ring ice on rock shards (i.e, already differentiated), and exit the rings with possibly high eccentricities and obliquities (Charnoz et al. 2011). These conditions could lead to significant tidal heating, although end-to-end modeling of the moons’ internal evolution from formation to their current location remains to be performed. This formation model might be particularly relevant to Miranda: it could explain the moon’s very low density compared to the other large moons, and provide a mechanism for explaining the moon’s internal differentiation, if confirmed by a

future mission.

These scenarios are summarized in Table 2 with a qualitative assessment of their implications for various aspects of the moons’ compositions and heat budgets. Some of these models are notional at this stage and end-to-end modeling from formation to the present remains to be performed. In particular, the early internal evolution of ring-sourced moons exiting the rings has not been investigated.

Origin	<sup>26</sup> Al Heat	Supervolatiles	Clathrates	Tidal Heating	Porosity
CPD				Depends on formation distance	
Impact Ejecta				Depends on formation distance	
Rings		Depends on ring progenitor	Depends on ring progenitor		

None/Unlikely	Some	Likely important	Major source
---------------	------	------------------	--------------

Table 2. Summary of heat sources and insulating material available to the large Uranian moons based on their origin. Objects accreted in the rings would form late but benefit from significant tidal heating in their early history whereas objects formed in the CPD might accrete early enough to benefit from short-lived radioisotope decay. Non-water ices such as CO<sub>2</sub> and NH<sub>3</sub> contribute to the formation of brines and can decrease the ocean freezing point. A formation from Uranus ejecta leads to a limited heat budget overall.

### 5.2 Models with Porous Core

Although a high porosity for the cores of Ariel, Umbriel, Titania, and Oberon is deemed unlikely (Section 4.1), Ceres and Enceladus have rocky cores with relatively low densities, between 2400 and 2800 kg/m<sup>3</sup> in the case of Ceres (Ermakov et al. 2017; Mao and McKinnon 2018) and about 2400 kg/m<sup>3</sup> for Enceladus (Hemingway and Mittal 2019) that indicate 13 to 35% porosity (Choblet et al. 2017; Melwani Daswani and Castillo-Rogez 2022). Likewise, the depth to Rhea’s rocky core appears no greater than 300 km (Tortora et al. 2016), implying a rocky core density lower than 2350 kg/m<sup>3</sup>. Because the Uranian moons are in the same size range as these bodies, albeit with a higher rock (i.e., radiogenic heat) content than Rhea, their cores might also contain porosity filled with ice or brine fluid.

Following their work on the Saturnian satellites (Neveu and Rhoden 2019), Neveu and Rhoden (personal communication) assumed a core density of 2400 kg/m<sup>3</sup> for the Uranian moons due to 25 vol.% fluid-filled porosity. In the case of a porous core with a density of 2400 kg/m<sup>3</sup>, the thin hydrosphere (e.g., 170 km in Ariel) would lead to rapid freezing of the hydrosphere. However, Neveu and Rhoden find that brines could be preserved in the core over several 100s km thanks to tidal heating, per analogy with Enceladus. These authors find

that this is likely the case for Ariel and Umbriel but not in the other moons: Miranda is too small to preserve liquid, like in the solid core model, and Titania and Oberon are too far from their primary to benefit from significant tidal heating.

### 5.3 Constraints on the Past Tidal Heat Flows of Ariel and Miranda

We reexamine the heat flow of Ariel derived from flexure analysis in the context of our models. We compute the complex tidal Love number  $k_2$  for undifferentiated and differentiated interiors (see Section 3.5) with and without a deep ocean at present. We range the crustal thickness as well as the viscosity for the lower part of the crust below a 10-km thick conductive shell. The dependence of  $Q/k_2$  on shell thickness and viscosity is presented in Figure 9a. The  $k_2$  for oceanless interiors ranges from  $3.8 \times 10^{-3}$  (frozen) to  $4.7 \times 10^{-3}$  (warm). The upper bound matches the results from Hussmann et al. (2006). Values for  $k_2$  are found to be between  $1.6$ – $16.4 \times 10^{-2}$  when an ocean is present. The  $Q$  values range from 20 to 1500 over the set of models. Figure 9 shows that the range of heat flow derived from geological analysis can be explained if a deep ocean is present and the shell viscosity was of the order of  $10^{14}$  Pa s. This implies that the moon held an ocean at the time of a recent MMR, potentially the 5:3 MMR with Umbriel (Cuk et al. 2020), or that enhanced tidal heating resulting from the increased eccentricity triggered melting and internal differentiation.

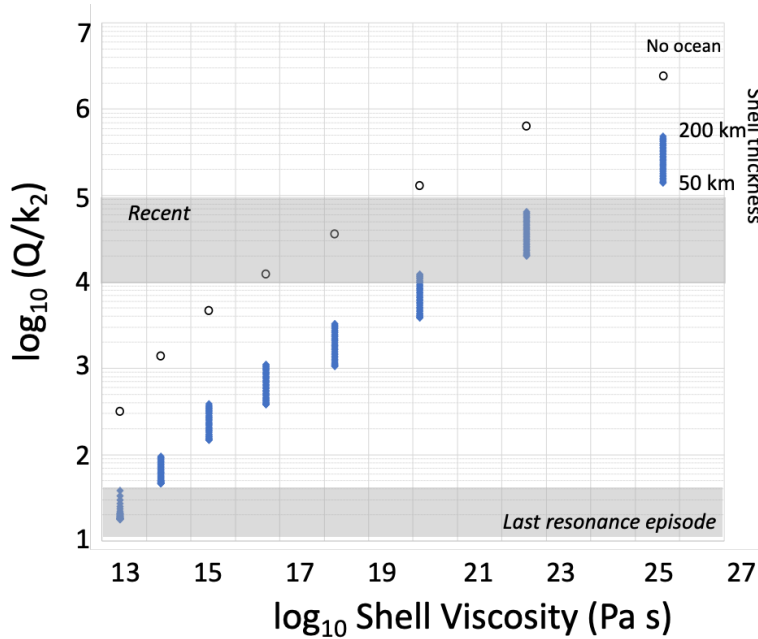


Figure 9a.  $Q/k_2$  for three-layer models of Ariel (rocky core at  $3060 \text{ kg/m}^3$ , ocean, and ice shell, closed circles) and ocean-less models (open circles) as a function of shell viscosity and thicknesses. The  $Q/k_2$  ranges estimated in the

literature are presented in gray boxes (Cuk et al. 2020 for recent  $Q/k_2$ ; Peterson et al. 2015 for geology-derived  $Q/k_2$ ).

A similar analysis carried out for Miranda shows that the  $Q/k_2 \sim 10^2$ - $10^3$  suggested by Cuk et al. (2020) at the time of the Ariel-Umbriel 5:3 MMR also requires the presence of a deep ocean and warm shell (viscosity  $\sim 10^{14}$  Pa s). This supports the Cuk et al. (2020) suggestion that Miranda’s ice melted during that phase and explains the high heat flow inferred by Beddingfield et al. (2015) from their investigation of Arden Corona.

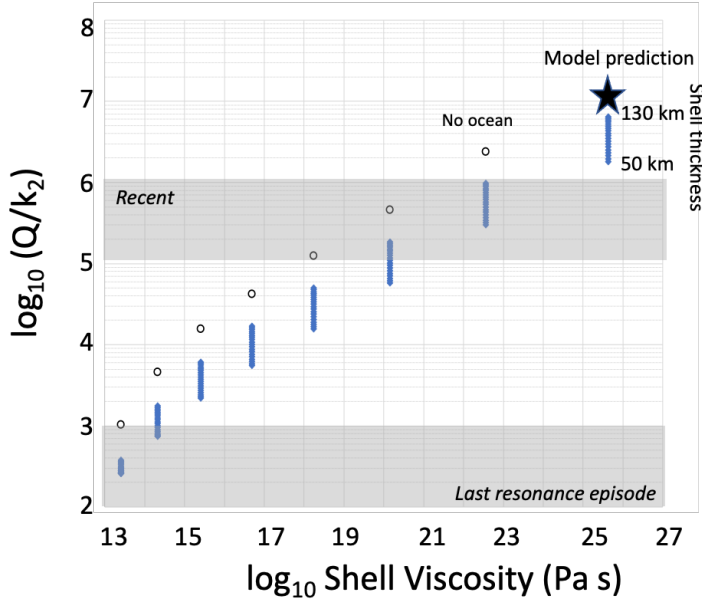


Figure 9b. Same as Fig. 9a but for Miranda. The star represents the  $Q/k_2$  derived from the current state of Miranda predicted by our models.

The  $Q/k_2$  ranges come from Cuk et al. (2020) for recent  $Q/k_2$  and Beddingfield et al. (2015) for geology-derived  $Q/k_2$ .

#### 5.4 Constraints on Interior Structures from Tidal Evolution Since Resonance

We assess whether our interior predictions could be consistent with the  $Q/k_2$  ranges estimated for each moon by Cuk et al. (2020) (Table 1). These estimates are based on the extent of eccentricity decay since the moons evolved out of mean motion resonances supposedly about 1 Ga based on the age inferred for Miranda’s coranae and Ariel’s surface (Zahnle et al. 2003; Kirchoff et al., 2022). As pointed out by Cuk et al. (2020), resonance timing is highly dependent on Uranus’  $Q/k_2$ , which may be frequency dependent (Fuller et al., 2016). Also,  $Q/k_2$  is averaged over the period of time since the moons broke out of their respective resonances. Hence, that parameter could have been smaller in the past and is higher at present. In practice, shortly after the moons left reso-



nances, their eccentricities are expected to damp over  $<100$  My (Tittlemore et al. 1993), yielding a drop in tidal heating and leading to internal freezing until eccentricity decay became very slow. Hence, the  $Q/k_2$  inferred by Cuk et al. (2020) for an evolution timescale of 1 Gy are representative of the moons’ current states. Since the moon’s geological activity is likely triggered by enhanced tidal heating, refined constraints on resonance timing may be obtained through future geological observations (e.g., crater-based dating) using the most recent impact flux models.

$Q/k_2$  are presented for three-layer models (rocky core, ocean, ice shell) as a function of ice shell thickness and ice shell viscosity. The shell thickness determines the volume of material that may be dissipating, depending on viscosity. Thin shells are prone to high deformation as a consequence of tidal forcing but may host little tidal dissipation. Thicker shells may deform less but offer a greater dissipative volume depending on viscosity. As a result, all results show that for three-layer models,  $Q/k_2$  varies by only one order of magnitude over the range of shell thicknesses determined for each moon. We also show results for models without a liquid layer. The latter results were vetted against the results from Hussmann et al. (2006).

The Cuk et al. study is not exhaustive and other interpretations for  $Q/k_2$  are possible. For example, simulations of coupled thermal-orbital evolution with the model of Neveu & Rhoden (2019) yield present-day values of  $Q/k_2$  of order  $10^3$  for Titania and Oberon with an ice shell surrounding a rocky core with 25 vol.% warm ice (175–270 K), and  $10^3$ – $10^5$  for Ariel and Umbriel in which part of the water in the core is liquid. These values are similar to the estimates of Cuk et al. (2020). For both those models and for the  $Q/k_2$  estimates presented in this section, obliquity-driven tides are not accounted for.

#### *Miranda*

Cuk et al. (2020) find a  $Q/k_2$  between  $10^5$  and  $10^6$  for Miranda. As shown in Figure 9b, a deep ocean cannot be ruled out but the shell viscosity has to be greater than  $10^{21}$  Pa s. In the absence of an ocean,  $k_2 \sim 1.9 \times 10^{-3}$  and therefore the dissipation factor is between 50 and 500, which allows for a warmer shell of up to  $\sim 210$  K. We plotted (star) the  $Q/k_2$  corresponding to the current state predicted by our models (see Figures 4 and 5). It is greater than the Cuk et al. estimate by one order of magnitude. This could imply that Miranda is warmer than predicted by our models, or could reflect the various uncertainties in this study (tidal heating not accounted for) and the Cuk et al. analysis (e.g., constant  $k_2/Q$  for Uranus).

#### *Ariel and Umbriel*

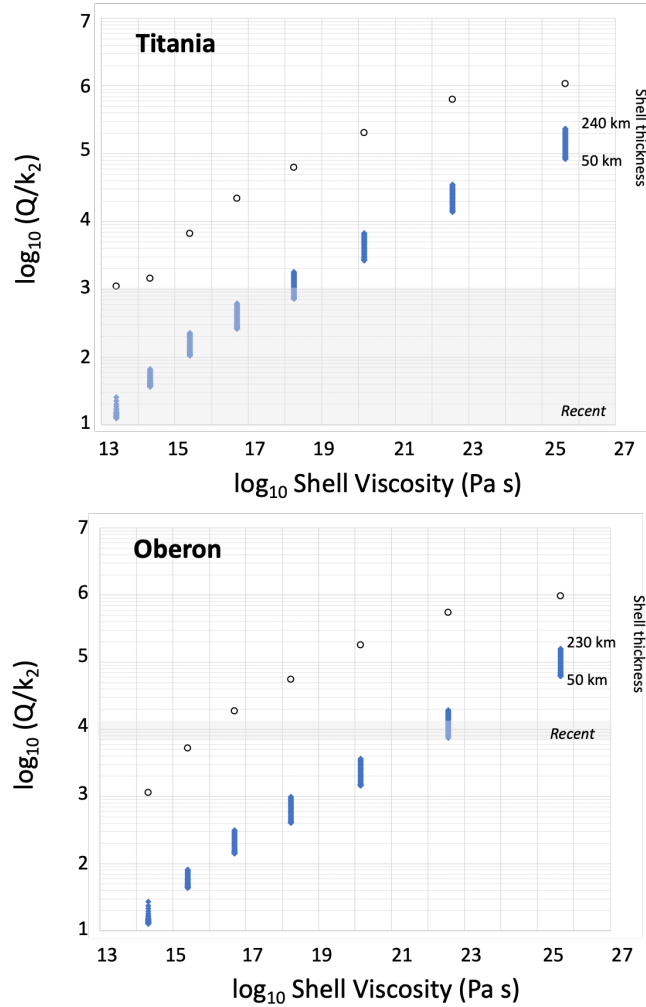
For Ariel, Cuk et al. (2020) infer  $Q/k_2$  between  $10^4$  and  $10^5$ , assuming the moon broke from resonance with Umbriel about 1 Gya. Figure 9a shows that this range can be explained by a high-viscosity shell ( $>3 \times 10^{22}$  Pa s) corresponding to a temperature  $<150$  K. The presence of an ocean a few tens of kilometers thick is consistent with these estimated values of  $Q/k_2$ . An alternative interpre-

tation has no ocean but a warm shell ( $Q$  of  $\sim 20$ -200 corresponding to a viscosity  $< 2 \times 10^{15}$  Pa s). For this kind of viscosity, an ice shell would be convecting and could lead to rapid freezing, hence this kind of model may not be sustainable over long timescales.

The same reasoning applies to Umbriel (same  $Q/k_2$  derived by Cuk et al. as for Ariel). The moon's large eccentricity (three times that of Ariel) indicates low tidal heating and is commensurate with Umbriel's greater orbital distance with respect to Ariel.

### *Titania*

Cuk et al. (2020) pointed out that the constraint of  $Q/k_2 < 10^3$  inferred from its dynamical evolution to explain Titania's current eccentricity suggests the presence of a deep ocean (Figure 10). In absence of a deep ocean, Titania's  $k_2$  is  $\sim 0.004$ , leading to  $Q < 4$ . This would correspond to a shell viscosity of  $3 \times 10^{13}$  Pa s that is difficult to reconcile with thermal evolution models, Titania's tidal dissipation state, and its surface geology. On the other hand, the presence of a deep ocean increases  $k_2$  by one order of magnitude with respect to an oceanless model while yielding  $Q$  values that are more consistent with the thermal evolution models reported in this study. For example, the model of Titania presented in Figure 4 has a  $k_2 \sim 0.24$  and  $Q \sim 140$  or  $Q/k_2 \sim 600$ .



*Oberon*

Similar reasoning applies to Oberon, for  $Q/k_2 \sim 10^4$  inferred by Cuk et al. (2020). A residual ocean in Oberon is as likely as in Titania considering their shared physical properties. However, a difference of one order of magnitude between the  $Q/k_2$  values for Oberon and Titania translates into a greater viscosity (order  $10^{21}$ - $10^{22}$  Pa s). Ocean-less models of Oberon's interior can match  $Q/k_2 \sim 10^4$  if the average shell viscosity is about  $5 \times 10^{15}$ - $5 \times 10^{16}$  Pa s. A warm shell at present is unlikely due to the limited heat production from long-lived radioisotopes and tidal heating corresponding to  $Q/k_2 \sim 10^4$  is «1 MW.

Figure 10. Same as Figure 9 but for Titania and Oberon. In the case of Titania, the low  $Q/k_2$  derived by Cuk et al. (2020) strongly suggests the presence of a deep ocean.

## 6. Observables for Future Mission

We discuss observations that may be carried out by a future spacecraft mission to investigate the extent of differentiation of the Uranian moons and search for deep oceans in these bodies. We focus on geophysical observations but also discuss possible compositional observations.

### 6.1 Interior Structure from Gravity and Shape Observations

The extent of differentiation can be inferred from the polar moment of inertia,  $C$ , via measurements of the triaxial shape and degree-two gravity coefficients under the assumption of hydrostatic equilibrium. It is important to note that the current uncertainties on the GM and mean radii for all the moons are large. The results presented below assume mean values for these parameters. Refining them should be a top priority of a future mission, as recommended by the Uranus Orbiter and Probe mission (NASEM 2022).

To estimate degree-2 gravity and shape parameters, we assume the bodies are relaxed to hydrostatic equilibrium. This allows the use of the Radau-Darwin approximation [e.g., Zharkov et al. (1985)]. Under this assumption, gravity and shape are determined by the rotation parameter ( $q = {}^2R^3GM$ ) and orbital properties. Then, the three shape radii are computed with:

$$a = R ( 1 + 7/6 q ) ( k_s + 1 )$$

$$b = R ( 1 - 1/3 q ) ( k_s + 1 )$$

$$c = R ( 1 - 5/6 q ) ( k_s + 1 )$$

and

$$J_2 = 5/6 q k_s$$

$$C_{22} = 1/4 q k_s$$

where  $k_s$  is the secular tidal Love number related to the normalized moment of inertia via:

$$k_s = ( 4 - Q ) / ( 1 + Q )$$

$$\text{with } Q = [ -5/2 ( 3/2 \times C/MR^2 - 1 ) ]^2$$

We use the normalized moment of inertia  $C/MR^2$  where  $M$  is the mass of the moon. The relationship between  $C/MR^2$  and interior structure properties are presented in Figure 11 for two-layer models with a rocky core and hydrosphere (which encompasses an ocean if present and icy shell). Due to limited constraints on layer properties, a single value of  $C/MR^2$  corresponds to a broad range of interior structures. In particular, the unknown shell density, which is determined by the relative fractions of porous undifferentiated material and water ice, introduces degeneracies when interpreting  $C/MR^2$  in terms of interior structure. Hence, a precision of  $\pm 0.005$  on  $C/MR^2$  leads to a precision on the hydrosphere thickness no better than  $\pm 50$  km for all the moons but Miranda. In the latter case, a precision of  $\pm 0.005$  on  $C/MR^2$  narrows the uncertainties on the hydrosphere density to  $< 50 \text{ kg/m}^3$  and thickness to  $\pm 15$  km.

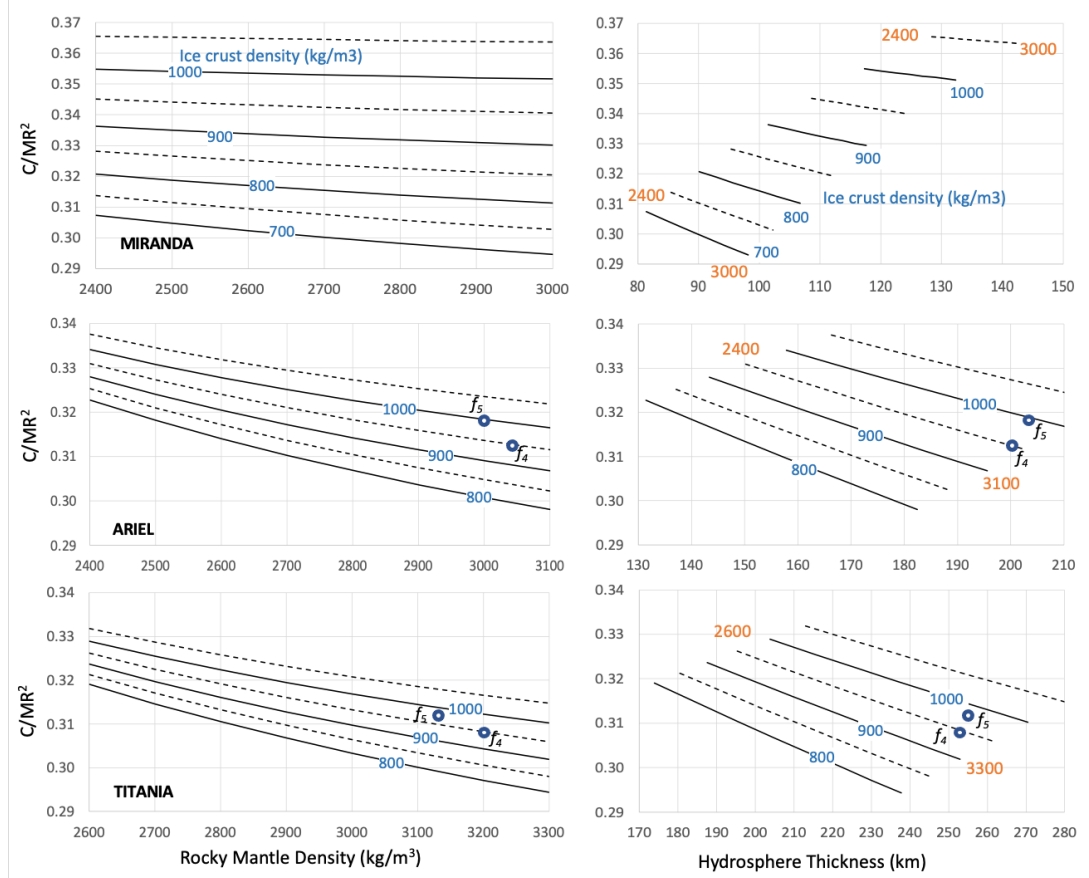


Figure 11. Estimates of the normalized polar moment of inertia  $C/MR^2$  as a function of the rocky core density, hydrosphere thickness, and hydrosphere density for two-layer model of Miranda, Ariel (also a proxy for Umbriel), and Titania (proxy for Oberon). Due to Miranda's low bulk density, the  $C/MR^2$  is primarily influenced by the hydrosphere density, while that parameter is primarily driven by core properties in the other cases. The circle point to specific examples represented in Figure 4 ( $f_4$ ) and 5 ( $f_5$ ). This figure covers a wide range of crust density, including highly porous ice ( $<900$  kg/m<sup>3</sup>) that might correspond to a formation in the rings. This might be refined by future models investigating the evolution of the moons after they've exited the rings.

The dependence of the degree-two longitudinal gravity coefficient,  $C_{22}$ ,<sup>1</sup> and the difference between equatorial and polar radii ( $a-c$ ) on rock density and mean density are presented in Figure 12 for all the moons and the parametric space covered in Figure 11. These parameters are also estimated for uniform interiors

<sup>1</sup>  $J_2$  can be inferred from  $C_{22}$  under the assumption of hydrostatic equilibrium,  $J_2 = 10/3 C_{22}$

(circles on right axes). Testing if the moons are differentiated or undifferentiated using shape data requires measuring  $(a-c)$  with a precision better than 1.15 km in the case of Miranda, and Ariel, 0.44 km for Umbriel, 0.13 km for Titania, and 0.05 km for Oberon. The latter case corresponds to measurement requirements on each shape axes of better than 20 m. Previous multi-flyby missions (e.g., Cassini) show that this kind of measurement is challenging (e.g., Thomas et al. 2010). Seeking information on the extent of differentiation sets even more stringent constraints. A  $\pm 0.005$  requirement on the determination  $C/MR^2$  translates into a measurement requirement on  $(a-c)$  of about  $\pm 0.060$  m.

Additional constraint on internal structure can also be sought in the degree-two gravity harmonics. Figure 12 shows that distinguishing between a differentiated and undifferentiated interior requires a precision on  $C_{22}$  better than  $6 \times 10^{-4}$  m/s<sup>2</sup> at Miranda and  $9 \times 10^{-6}$  m/s<sup>2</sup> at Oberon (or 60 mgal and 0.7 mgal, respectively).

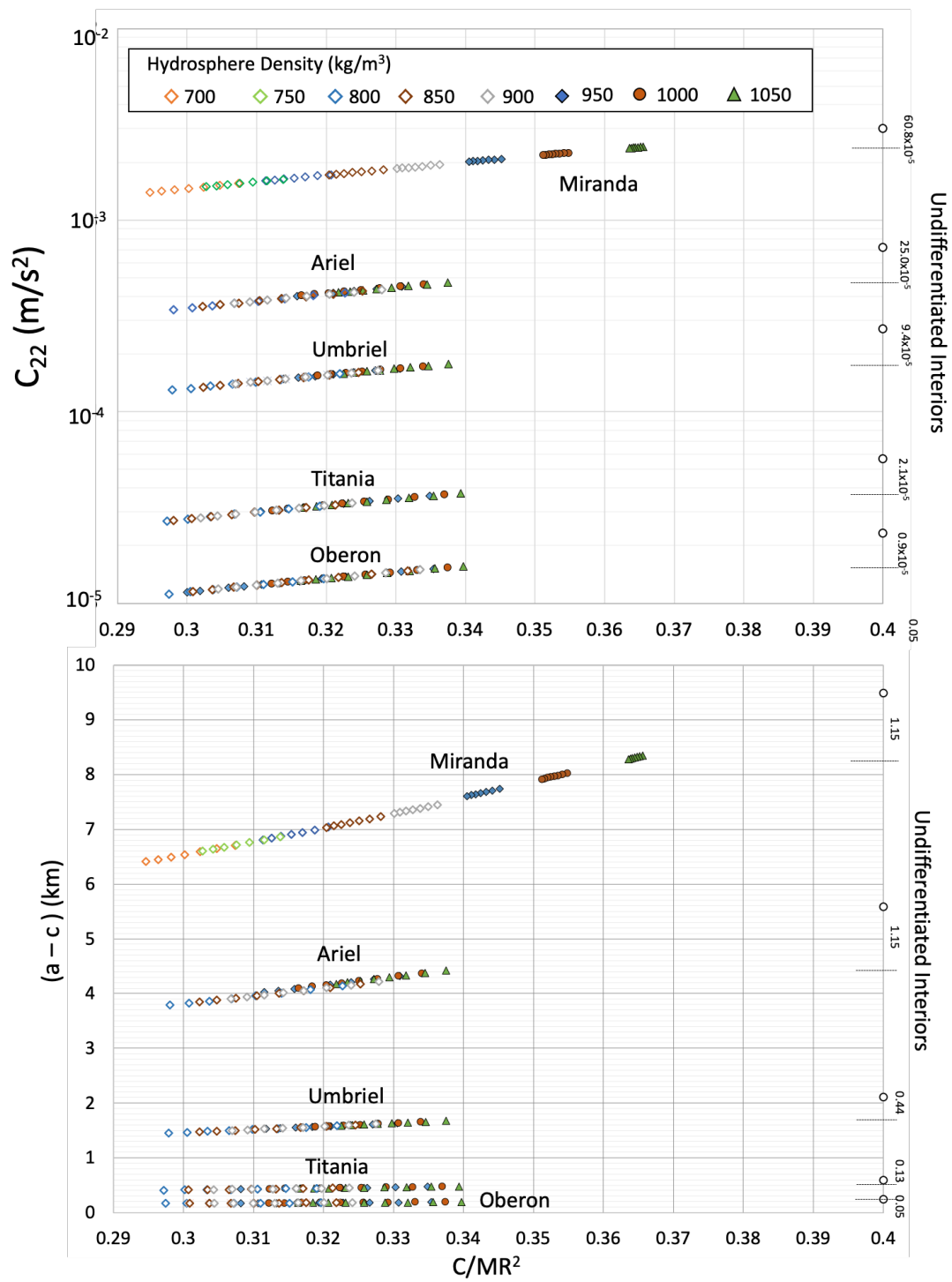


Figure 12. Estimates of the moon’s (a-c) and degree-two gravity coefficient  $C_{22}$  under assumption of hydrostatic equilibrium for the two-layer models presented in Figure 11 and for uniform interiors (open circles on right). Numbers on the right-hand side represent the separation between uniform models and differentiated models in  $\text{m/s}^2$  for  $C_{22}$  and km for (a-c).

Acquiring shape data and degree-two gravity harmonics can lead to independent estimations of  $C/MR^2$  and to detection and quantification of non-hydrostatic anomalies. Departure from hydrostatic equilibrium has been frequently found at bodies in the  $<1500$  km size class. Non-hydrostatic anomalies can take the form of a frozen, fossil shape [e.g., Iapetus (Castillo-Rogez et al. 2007)] or a core shape anomaly [as found at Enceladus (McKinnon et al. 2007)]; sometimes, no explanation can be found [e.g., Ceres (Park et al. 2016) or Rhea (Tortora et al. 2016 and references therein)]. Hence, gathering both gravity and shape information on the global properties of the moons can increase the level of confidence in the determination of their internal structures.

## 6.2 Detectability of Liquid Layers by Magnetic Induction

### 6.2.1 Ocean Electrical Conductivity

We distinguish the cases when the ocean temperature is at the water freezing temperature (hereafter referred to as “warm” ocean) and colder oceans sustained by the eutectic/peritectic of antifreeze solutes, in particular  $\text{NH}_3$  and chlorides.

For the “warm” ocean cases, the residual ocean is dominated by  $\text{NH}_4^+$ ,  $\text{Cl}^-$ ,  $\text{CO}_3^{2-}$ ,  $\text{HCO}_3^-$  as well as other cations (in particular  $\text{Na}^+$  and  $\text{K}^+$ ) (Figure 13). The presence of bi/carbonates and ammonium ions increases EC beyond the contribution of major elements leached from rock (CR22). The ionic strengths of the solutions are between 0.8 and 1.5 mol/kg, hence approaching or exceeding the applicability limit of the McCleskey et al. (2012) model. Analog solutions observed at a soda lake such as Mono Lake (Jellison et al. 1999) indicate an EC of the order of 8 S/m at 298 K or  $\sim 4.5$  S/m at 273 K. This is only a rough estimate and experimental measurements of relevant solutions are needed in order to provide support to future missions.



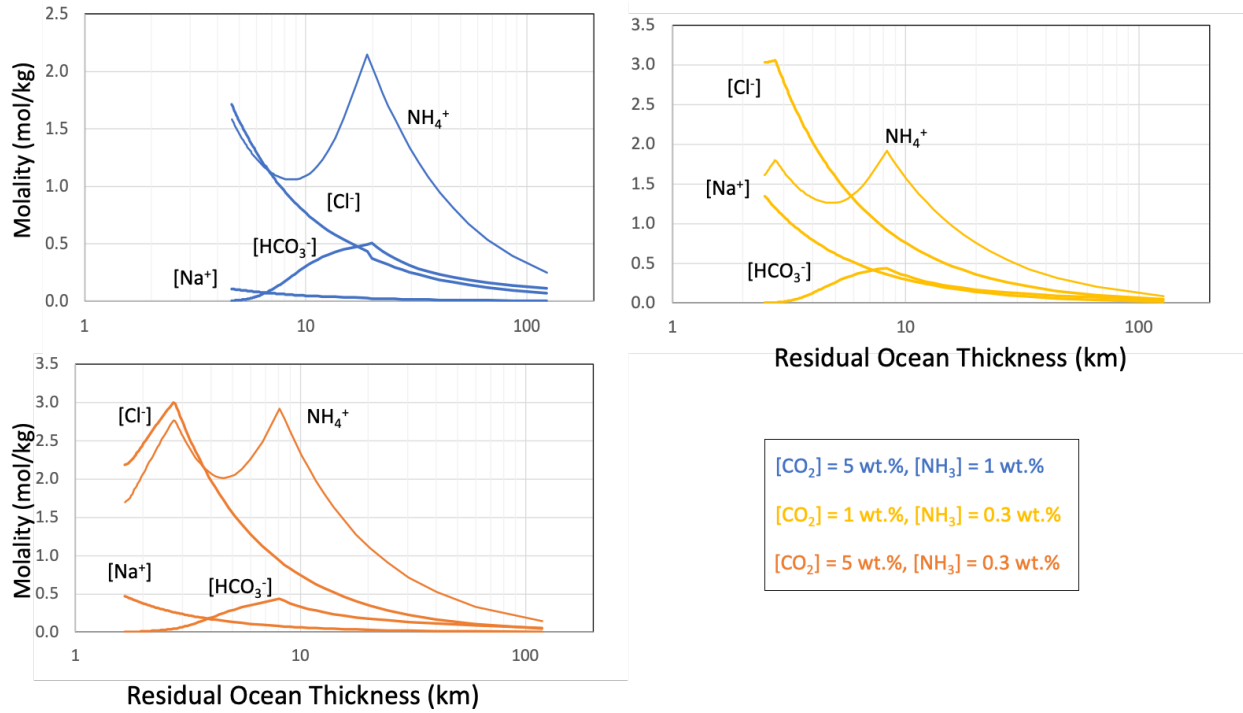


Figure 13. Concentration of key species driving the EC of residual oceans in Uranus' large moons. Besides  $\text{NH}_3$ , residual oceans are dominated by sodium chloride and sodium bicarbonate.

For residual layers below the water freezing temperature, the temperature could be theoretically as low as 176 K, the water-ammonia peritectic (our FREZCHEM simulations stop converging at about 185 K). At that point, the residual layer thickness is between 1-3 km. Electrical conductivity data are lacking for cryogenic brines. Assuming that the temperature correction coefficient of  $\sim -0.02/\text{K}$  is applicable at temperatures below 255 K (see Section 3.7), the EC of chloride-rich solution would tend toward 0 S/m around 245 K or a thickness between 3-10 km. Below  $\sim 245$  K, a brine layer may be present without exhibiting an induced field signature. Other solutes could contribute to increasing the conductivity but low-temperature EC estimates are missing for compositions with a large fraction of  $\text{HCO}_3^-$  and  $\text{Na}^+$ .

#### *Electrical Conductivity of Brine-Filled Porous Rock*

For a porosity of 0.3 and a brine EC of up to 30 S/m at  $100^\circ\text{C}$  (e.g., Ucock et al. 1980), we find an effective EC of brine-filled porous rock between 2.5 S/m and 8 S/m. This range is derived from empirical observations by Saner and Kissami (2003) who have measured the macroscopic conductivity as a function of the brine conductivity for a wide range of rock and porosity configurations. It

reflects in particular the permeability of the samples: higher permeability leads to higher EC values. For porous brine EC approaching 50 S/m, the macroscopic conductivity is between 1 and 2 S/m.

The two moons in which porous cores might preserve brines until present are Ariel and Umbriel, for core radii of  $\sim 410$  km and  $\sim 420$  km, respectively. Neveu and Rhoden (personal communication) do not find any liquid preserved in the cores of Miranda, Titania and Oberon at present.

### 6.2.2 Detection of Induced Field

The presence of salty bodies of liquid water on the major moons can be inferred from measurements of its inductive response to the time-varying Uranian magnetospheric field (Arridge and Eggington 2021, Cochrane et al. 2021, Weiss et al. 2021). In particular, it has been found that the synodic frequency of the Uranian field at each of the major moons (as well as the second and third harmonics at Miranda and second harmonic at Ariel) would generate time-varying electrical currents whose maximum induced surface magnetic field amplitude should exceed the sensitivity of typical spacecraft fluxgate magnetometers ( $\sim 1$  nT) assuming that the moons are perfect conductors.

More generally, here we consider 2- and 3-layer models like those in Section 3 in which either a porous conducting core is overlain by a nonconducting ice shell or a nonconducting core is overlain by a conducting relict ocean in turn overlain by a nonconducting ice shell. In particular, it has been previously shown that if Ariel contains either a 30-km-thick relict ocean with conductivity of  $15 \text{ S m}^{-1}$  or a porous, briny core with conductivity of  $2 \text{ S m}^{-1}$ , it should generate a detectable induced surface field (Weiss et al. 2021).

We expand the analysis of Weiss et al. (2021) by calculating the induction field for relict ocean and porous core models for all five major moons (Table 3). Following their approach, we calculate the time-varying field at each moon using the AH5 internal hexadecapole field model for Uranus in 1987 (Herbert, 2009). This provides a good approximation for the actual field experienced by the innermost three moons (Miranda, Ariel, and Umbriel), but only a first-order estimate of the field experienced by the outer moons Titania and Oberon, which are likely more affected by diurnal and seasonal effects associated with the interaction of the solar wind with the Uranian magnetosphere. For a more detailed study of the induction responses of the latter moons, we refer the reader to Arridge and Eggington (2021). Additionally we adopt more realistic assumptions for the briny core scenario. We reduce the conductivity to  $1 \text{ S m}^{-1}$  and limit the porous, conducting region of the core to an outer layer for all the moons apart from Miranda (see discussion in Section 4.1).

We find that the maximum induced field amplitude for the thickest relict oceans (e.g., 20-30 km) as well as the porous core structures should be detectable ( $1$  nT) during a nominal 100-km altitude spacecraft flyby with two exceptions. In the briny core scenario, the induced fields 100 km from Miranda and Oberon are  $< 1$  nT, owing to Miranda's small size and the weak driving field at Oberon.

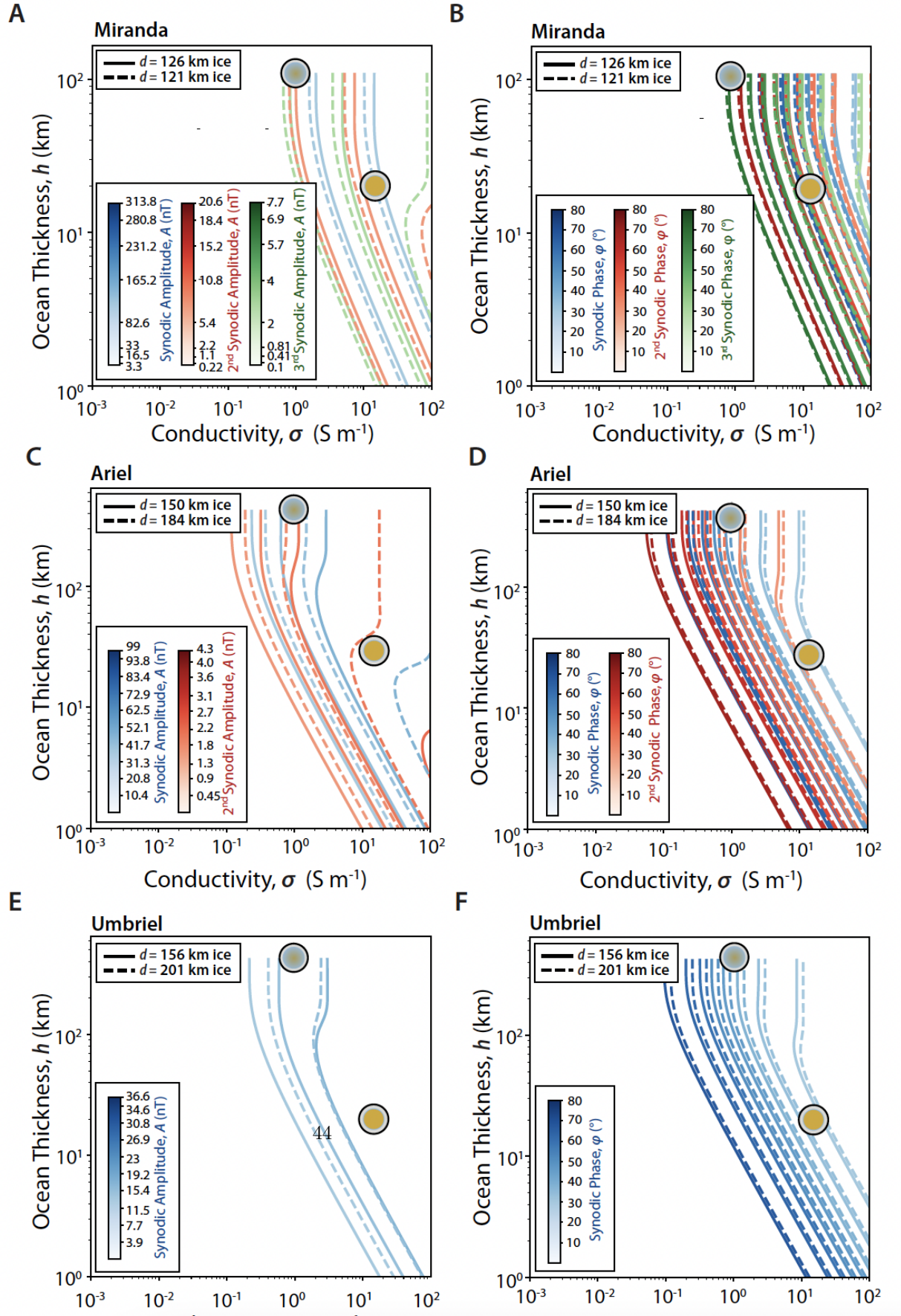
Signals from the porous cores are weaker than those of the relict oceans due to the cores' 15 times lower EC. This effect overwhelms the positive contribution from the 1.7–5times larger conducting layer thickness  $h$  at Miranda, Ariel, and Umbriel. This tradeoff between ocean conductivity and thickness illustrates the non-unique nature of the induction response. Each contour in Figure 14 represents a family of internal structures, with different ocean thicknesses and conductivities, producing the same induction amplitude or phase. When the driving magnetic field has oscillations at multiple frequencies, measuring the induced response at each frequency may break this degeneracy. This may be possible at Miranda and Ariel, where the magnetic oscillation at the second harmonic of the synodic frequency is significant. Additionally, measuring the phase delay of the induced response with respect to the driving field can aid characterization, including at the outer moons where only one frequency is available for magnetic sounding. In conjunction with restrictions on the range of plausible interiors from gravity, shape, and compositional measurements it may be possible to broadly characterize a subsurface ocean with a limited number of flybys (e.g., Weiss et al. 2021).

Table 3. Reference interior structures used for the induced field models presented in Figure 14. The symbol  $\sigma$  refers to the ocean electrical conductivity.

Moon	#1 - Relict ocean model Ocean conduc- tivity, = 15 S m <sup>-1</sup>	#2 - Briny core model Briny rock conduc- tivity, = 1 S m <sup>-1</sup>	#3 - Core model with porous layer Briny rock conduc- tivity, = 1 S m <sup>-1</sup>			
	Ice thick- ness, $d$ (km)	Ocean thick- ness, $h$ (km)	Ice thick- ness, $d$ (km)	Porous rock thick- ness, $h$ (km)	Ice thick- ness, $d$ (km)	Porous rock thick- ness, $h$ (km)
Miranda						
Ariel						
Umbriel						
Titania						
Oberon						

The non-detection of an induced field at a moon would not necessarily exclude

the presence of liquid. The conducting layer in either the relict ocean or porous core scenarios could be thinner than what is assumed here, reducing the induction response (Figure 15). Additionally, the liquid temperature could also be significantly below the water freezing temperature, such that the electrical conductivity would be much lower than the assumptions used here, to the point that a deep ocean might not be detectable at all.



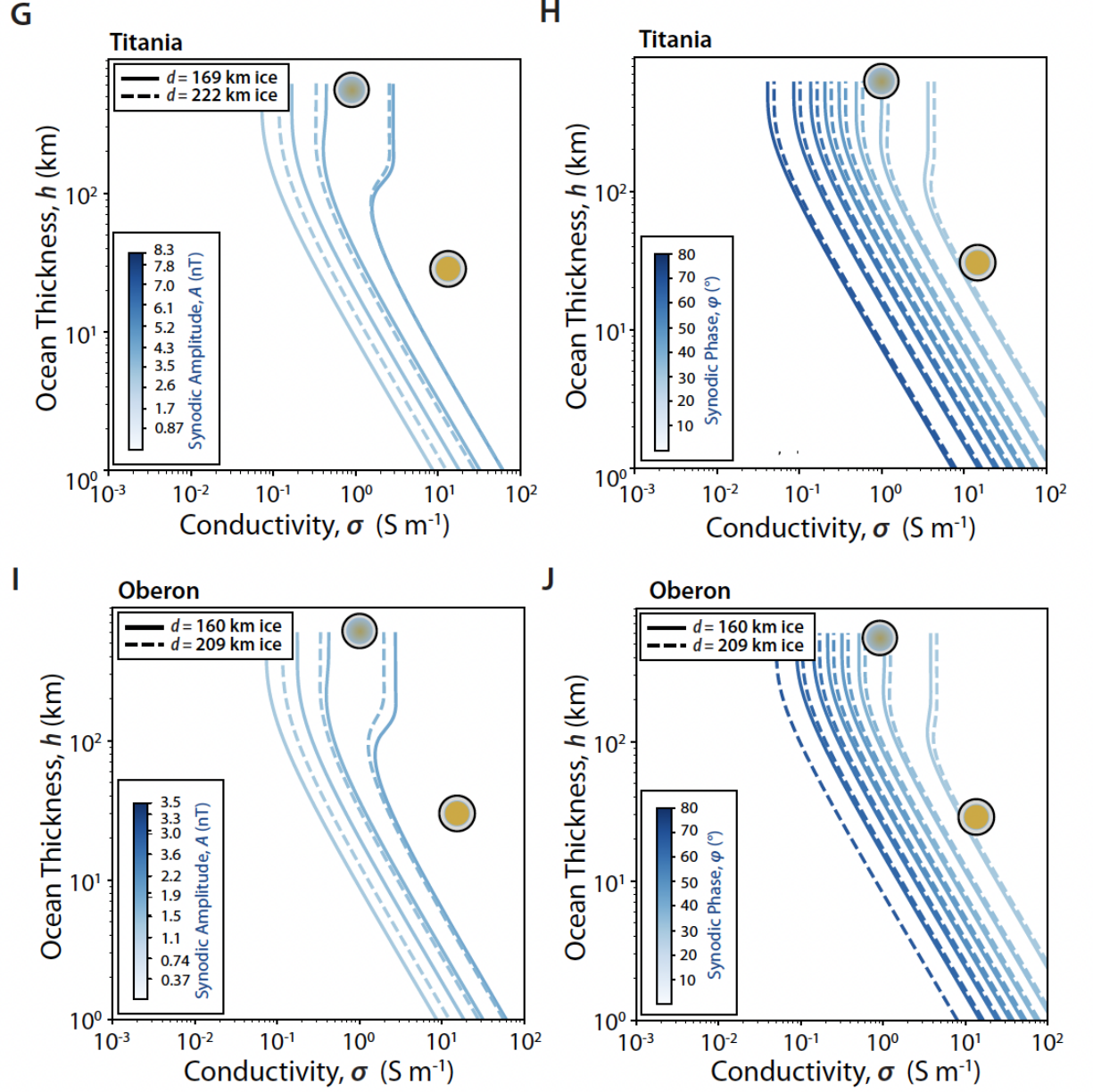


**Figure 14.** Induced fields at the synodic frequencies of the major moons. (A, C, E, G, I) Amplitude and (B, D, F, H, J) phase for various frequencies of the induced field at the surface induction pole for each moon. Solid and dashed curves denote models with two different ice shell thicknesses, corresponding to the relict ocean and briny core models (#1 and #2 in Table 3), respectively. Shown are the inductive responses to the first (red), second (blue) and third

(green) harmonics of the synodic frequency. Numerical values of contours correspond to labeled values on colorbars. Two icons denote briny core (upper left icon) and relict ocean (lower right icon) (see Table 3). (A, B) Miranda. (C, D) Ariel. (E, F) Umbriel. (G, H) Titania. (I, J) Oberon. Calculated using Uranus  $\text{AH}_5$  internal magnetic field model of Herbert (2009). The actual inductive response of Oberon and Titania is expected to differ from what is calculated here due to the effects of the solar wind and its dependence on diurnal and seasonal variations.

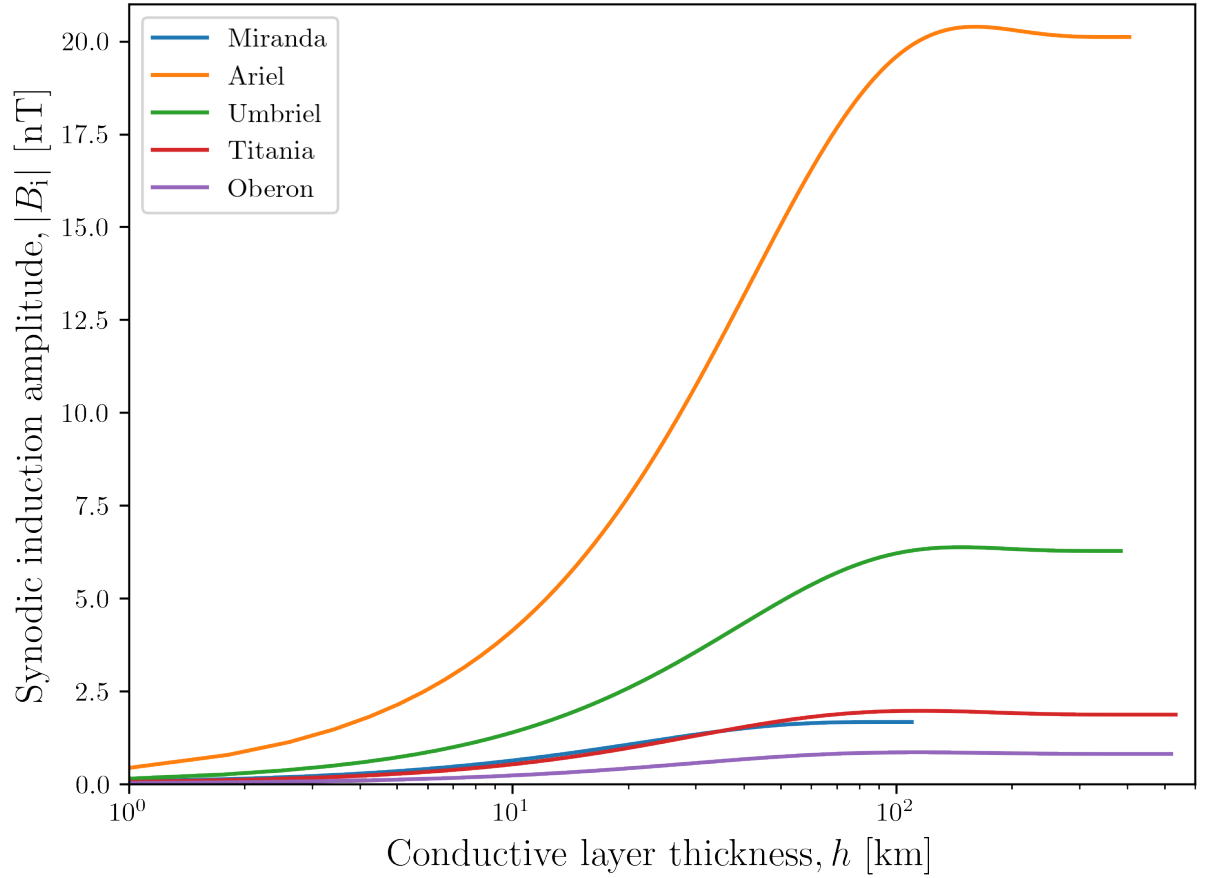


Figure 15. Maximum amplitude of the induced response to the synodic driving field at the surfaces of the major moons as function of the thickness of the porous, conducting layer in the moon's core. Each moon has a non-conducting ice shell with thickness defined for model #3 in Table 3.

### 6.3 Exposure of Deep Interior Material

If deep oceans are present in the large Uranian moons at present, then they are

likely thin (tens of kilometers) layers below a thick shell ( $>100$  km in Miranda and  $>200$  km in the other moons). As noted in the introduction, the reports of  $\text{NH}_3$ - or  $\text{NH}_4^+$ -rich deposits found at Miranda and Ariel may imply recent exposure. Per the ocean composition models presented in Section 4.3, a few to tens of km thick liquid layers may be enriched in  $\text{NH}_3$  and thus relatively buoyant with respect to an icy crust (Figure 7), especially if they contain dissolved gas. This system may be under pressure as a consequence of advanced freezing of the hydrosphere, as suggested for Ceres (Neveu and Desch, 2015). In these conditions,  $\text{NH}_3$ -based cryovolcanism is a possibility, as suggested earlier by Kargel (1991), although the actual mechanism for establishing communication between the surface and liquid at  $>150$  km depth remains to be investigated. The current basal heat flow at Ariel’s crust is of the order of  $1 \text{ mW/m}^2$  and might be too low to drive convection. Furthermore, if Ariel’s crust is convecting, then it is most likely in the stagnant lid regime (Stern et al. 2018). This applies to the other Uranian moons as well.

Transfer of deep ocean material via fractures (e.g., induced by impacts) or tectonic activity (e.g., extensional faulting) is another possibility, although porosity would close as a result of compaction creep at temperatures above  $\sim 170$  K, several tens of kilometers above the interface between the ice shell and the deep ocean. Alternative emplacement mechanisms may include impacts (excavation and ejecta) or mass wasting of oceanic material captured in the crust upon freezing. Heating produced by large impacts could drive the formation of shallow melt ponds that froze on a  $\sim 1$  My timescale (e.g., Bowling et al. 2019) and create localized concentration of salts trapped in the shell. Lastly, the features observed by Cartwright et al. (2020) in the 2.18 and 2.24 micron range could also result from the irradiation of  $\text{NH}_3/\text{CO}_2/\text{H}_2\text{O}$ /etc. substrates.

Spatially resolved reflectance spectra collected over Ariel could look for spatial associations between  $\text{NH}_3/\text{NH}_4$  and specific geologic features. Exposure via impacts would imply higher concentration of that material in fresher craters, similar to Charon (e.g., Grundy et al., 2016). Deeper sourcing from a residual ocean via fractures would lead to an association of these compounds with chasmata and double ridges. Upcoming observations with the NIRSpec spectrograph on the James Webb Space Telescope (program 1786, spanning 2.9 - 5  $\mu\text{m}$ ) will improve our understanding of the Uranian moons’ surface compositions but will not provide spatial context. Hence, both high-resolution imaging and infrared spectroscopy by a future spacecraft mission would confirm the nature of the material and test its association with craters, mass wasting features (e.g., landslides), or faults.

#### 6.4 Habitability Potential

Assessing the habitability potential of the large Uranian moons is an important goal stated by the Roadmap to Ocean Worlds (Hendrix et al. 2019) and UOP study (NASEM 2022). This knowledge would add to our understanding of the processes that drive the evolution of icy bodies in the 1000-km size range. A major question raised in these two references is about the nature of heat



sources that keep oceans worlds going. This question should be expanded to encompass the mechanisms that preserve internal heat by decreasing heat loss. Clathrate hydrates have been suggested as insulating material and inhibitor of convection (e.g., Castillo-Rogez et al. 2019; Kamata et al. 2019) but chemical modeling presented above suggests these compounds may not be favored in the environments hosted by the Uranian moons. If present, they would increase the shell densities to  $>1000 \text{ kg/m}^3$ ; however, their signature in the gravity (Figures 11 and 12) is likely to be overwhelmed by the contributions of other interior properties (or at least the gravity inversion will not be unique).

Porosity provides another means to decrease heat loss and could exhibit some signature in the geology. For example, Bland et al. (2022) point out that the relaxed morphology of Yangoor crater on Ariel cannot be explained by the radiogenic heat flow. Instead  $>60$  times higher heat flow sustained for hundreds of My or weaker thermomechanical properties of Ariel’s crust may be required. Bland et al. suggest a thick porous layer could insulate heat loss and increase the temperature of the lithosphere, a hypothesis that our modeling supports with the caveat that an episode of intense tidal heating could have led to significant creep-driven compaction. A future mission should aim at characterizing crater morphologies for a wide range of crater sizes in order to inform the thermophysical properties of the moons’ upper crusts.

If the occurrence of  $\text{NH}_3$  and  $\text{NH}_4$  compounds associated with recent geological features is confirmed at Ariel, then their relative concentrations could provide a rough estimate of the temperature regime of the ocean (Figure 7). This could prove a critical source of information if the ocean temperature is below  $\sim 245 \text{ K}$  and does not exhibit an induced magnetic field detectable by spacecraft. Incidentally, that temperature is close to the lower limit for metabolic activity and reproduction of terrestrial microbes, based on the current state of knowledge (see Clarke 2014; Cockell et al. 2016 and references therein). Hence, this kind of ocean may not be of great interest for astrobiology, although one cannot rule out that certain lifeforms may be able to thrive in this environment. In any case, the electrical conductivity of ammonium, carbonate, and chloride mixtures should be measured over a wide range of temperatures, down to  $\sim 240 \text{ K}$  in order to narrow down conditions under which liquid may be present but not carry a detectable magnetic field.

The relict oceans would be highly concentrated solutions because the starting composition of these bodies, if they formed in the Uranian CPD, was likely rich in  $\text{CO}$  and  $\text{CO}_2$  ices and  $\text{NH}_3$ , leading to  $\text{CO}_3\text{-NH}_4$ -rich compositions. Alternative formation models (i.e., Uranian ring origin) could lead to a feedstock depleted in volatiles but still involve chloride brines. The habitability potential of such briny environments with compositions not encountered naturally on Earth (e.g., high  $\text{NH}_3$  abundance) needs to be addressed in greater detail. In particular, this potential depends in part on the preservation of chemical gradients. The thick ice shells ( $>100 \text{ km}$ ) limit the flux of surface oxidants and therefore the flux of surface chemical energy available to any life (e.g. Hand et al.

2007) over the long term. On the other hand, radiolysis of water has been suggested as a possible mechanism for creating chemical gradients in porous rocky layers (Bouquet et al. 2017; Altair et al. 2018). In Titania and Oberon, the warmest models include a late phase of silicate dehydration that could replenish the residual ocean in oxidants, as simulated by Melwani Daswani and Castillo-Rogez (2022) in the case of Ceres. However, remote sensing techniques are limited in the number of minerals and ices they can tease out from the surface. Future near infrared (NIR) observations intended to address moon habitability should aim for both high spectral ( $<20$  nm) and spatial ( $\sim$ km scale) resolution in order to assay compounds that may be associated with recent geological features.

## 7. Summary

This study considered three sources of information for assessing the prospect that the Uranian moons currently host liquid water in their interiors: observational constraints about their internal and geological evolution, the current level of tidal heating, and thermal models. Based on the results presented in this study, we predict that Ariel, Umbriel, Titania, and Oberon could have preserved deep liquid until present, sustained by radioisotope decay heat combined with a decreased thermal conductivity of the outer shell that may be due to porosity (e.g., Neumann et al. 2020; Bierson and Nimmo 2022). Even then, the oceans predicted at present would likely be thinner than 30 km or confined to porosity in the upper part of the rocky core. However, these residual oceans could still be detectable by in situ magnetic probing, provided that their temperatures do not fall too much below the water eutectic ( $\sim 245$  K). Our models assumed conductive ice shells, and thus represent a favorable outcome in terms of heat transfer. One cannot rule out convection onset in these moons, at least for some periods in their evolution (see King et al. 2022).

A notable exception is Miranda. Despite its intriguing geology and candidate ocean world categorization by Hendrix et al. (2019), this study could not find scenarios that would preserve a deep ocean in that moon until present. The shape data returned by Voyager 2 suggests that Miranda is at least partially differentiated. However, differentiation cannot be explained by the scenarios simulated with the thermal evolution models presented here (CPD accretion  $>3$ - Myr after CAIs, no tidal heating). If confirmed, differentiation was likely triggered by an episode of intense tidal heating consistent with high heat flow signatures associated with some of the coronae (Beddingfield et al. 2015). Furthermore, the potential role of obliquity-driven tides, dynamic fluid tides, and mean motion resonances (Tyler 2014; Chen et al. 2014; Cuk et al. 2020) in heating Miranda should also be further explored in combination with its thermal evolution. Miranda could also have formed in conditions or circumstances different from those explored in this study, for example within the Uranian rings (Crida and Charnoz 2012; Hesselbrock and Minton 2019).

Ariel is particularly interesting as a future mission target because of the detection of  $\text{NH}_3$ -bearing species on its surface (Cartwright et al., 2021) that could

be evidence of recent cryovolcanic activity, considering these species should degrade on a geologically short timescale. Geologic features, visible in Voyager 2 ISS images of Ariel, show some evidence for cryovolcanism in the form of double ridges and lobate features that may represent emplaced cryolava (Beddingfield and Cartwright 2021). A future mission aimed at confirming the state of differentiation and presence of a deep ocean in Ariel would help put these surface observations in context. The largest moons, Titania and Oberon, are also expected to preserve a deep ocean with thicknesses of a few tens of kilometers. The presence of deep oceans is consistent with constraints on  $Q/k_2$  inferred from dynamical models (Cuk et al. 2020), as a possible but not unique interpretation. A stronger case can be made for Titania, whose low  $Q/k_2$  appears to require both a low  $Q$  and high  $k_2$  (i.e., a thick shell decoupled from the rocky core by a deep ocean), at least within the assumptions of the Cuk et al. study (e.g., assumed  $Q/k_2$  for Uranus).

Based on current understanding, we conclude that the Uranian moons are more likely to host residual or “relict” oceans than thick oceans. As such, they may be representative of many icy bodies, including Ceres, Callisto, Pluto, and Charon (De Sanctis et al. 2020). The detection and characterization (depth, thickness) of deep oceans inside the Uranian moons, Miranda and Ariel in particular, would help assess whether these bodies are benefiting from tidal heating from unknown origin (as was the case at Enceladus before the Cassini mission). Bounds on the timing of geological activity would bring independent information on the occurrence of tidal resonances. On the modeling side, future work should aim to model the implications of increased tidal heating due to resonance crossing on the global evolution of the moons.

On the other hand, if freezing is more advanced than envisioned in this study, a residual ocean temperature may fall below  $\sim 245$  K and may not exhibit an induced magnetic field detectable by spacecraft. In this case, evidence and nature of a deep ocean may be found in the exposure of deep ocean material, as suggested for Ariel, and maybe Miranda. In any case, the electrical conductivity of ammonium, carbonate, and chloride mixtures should be measured over a wide range of temperatures, down to  $\sim 240$  K in order to narrow down conditions under which liquid may be present but not carry a detectable magnetic field.

Testing for the presence of deep oceans in the Uranian moons and their communication with the surface would increase our understanding of the processes preserving liquid reservoirs in icy moons  $< 1000$  km in diameter, with plausible applications to dwarf planets across the Solar System.

### Acknowledgements

Part of this work was carried out at the Jet Propulsion Laboratory, California Institute of Technology, under a contract with the National Aeronautics and Space Administration (80NM0018D0004). ©2022. All rights reserved.

The authors acknowledge discussions with Karl Mitchell and Francis Nimmo. M. N. was supported by the CRESST II agreement between NASA GSFC and

Univ. Maryland, College Park (award number 80GSFC17M0002). B. P. Weiss thanks the NASA NASA Jet Propulsion Laboratory (JPL) (consulting services agreement #1662407) for support. J. B. Biersteker thanks the NASA Europa Clipper Project (University of Michigan/JPL SUBK00011438) for support.

### Data Availability Statement

This work uses physical and dynamical properties for the Uranian moons from NASA’s Solar System Dynamics website: <https://ssd.jpl.nasa.gov>. The physical properties (shape radii and GM) are the values adopted by the International Astronomical Union (Archinal et al. 2018).

All other parameters used for the models come from published references or are in the public domain.

Models outputs (csv files) will be made publicly available in Zenodo. The corresponding DOI will be provided in the revised version of the manuscript.

## APPENDIX

### Appendix A Perple\_X models

**Table A.1** Bulk compositions used in Perple\_X models. The composition of Comet 67P/Churyumov-Gerasimenko is a synthesis from Pätzold et al. (2016), Dhooghe et al. (2017), Le Roy et al. (2015) and Bardyn et al. (2017), and using a dust-to-ice mass ratio of 4:1, as inferred by Pätzold et al. (2016). The CI chondrite composition was obtained from the compilation by Palme et al. (2014).

Element	Comet 67P/C-G	CI chondrite
	Wt. %	Wt. %
H	11.4	2.02
C	27.08	3.56
N	1.03	-
O	41.06	45.96
K	0.03	0.06
Mg	0.99	9.80
Al	0.18	0.87
Si	10.54	10.95
S	1.81	5.47
Ca	0.08	0.94
Fe	6.10	18.93

### APPENDIX B - Radioisotope Decay Parameters

The present-day ( $t=4.56$  Gy after CAI-formation) long-lived radiogenic heating rate per unit mass of rock is the sum  $\Sigma (X_i H_{oi} \ln(2)/t_{1/2} \exp[-\ln(2) t/t_{1/2}])$  with

$H_0$  representing decay energy,  $t_{1/2}$  half-life, and  $X_i$  abundances per kg of rock for each isotope  $i$ . Parameter values are provided in Table B.1. his represents about  $5 \times 10^{-12}$  W/kg of rock.

**Table B.2** Isotope concentrations and decay parameters used in this study. Isotope parameters are from Van Schmus (1995) for the long-lived radioisotopes and Castillo-Rogez et al. (2009) for  $^{26}\text{Al}$ . Elemental abundances for a CI chondrite compositions are  $[\text{U}] = 0.00816$  ppm,  $[\text{Th}] = 0.0298$  ppm,  $[\text{K}] = 539$  ppm,  $[\text{Al}] = 8370$  ppm (Lodders 2021).

Species $i$	Isotope fraction (wt.%) of element at present	Decay heat production $H_0$ (W/kg)	Half Life $t_{1/2}$ (year)
$^{26}\text{Al}/^{27}\text{Al}$	$5 \times 10^{-5}$	$3.57 \times 10^{-1}$	$7.16 \times 10^5$
$^{40}\text{K}/^{39}\text{K}$		$29.17 \times 10^{-6}$	$1.277 \times 10^9$
$^{238}\text{U}/\text{U}$		$94.65 \times 10^{-6}$	$4.47 \times 10^9$
$^{235}\text{U}/\text{U}$		$568.7 \times 10^{-6}$	$7.0381 \times 10^8$
$^{232}\text{Th}/\text{Th}$		$26.38 \times 10^{-6}$	$14.01 \times 10^9$

## APPENDIX C - Thermal Metamorphism

The figure below summarizes the outcomes of Titania’s rocky core thermal evolution.

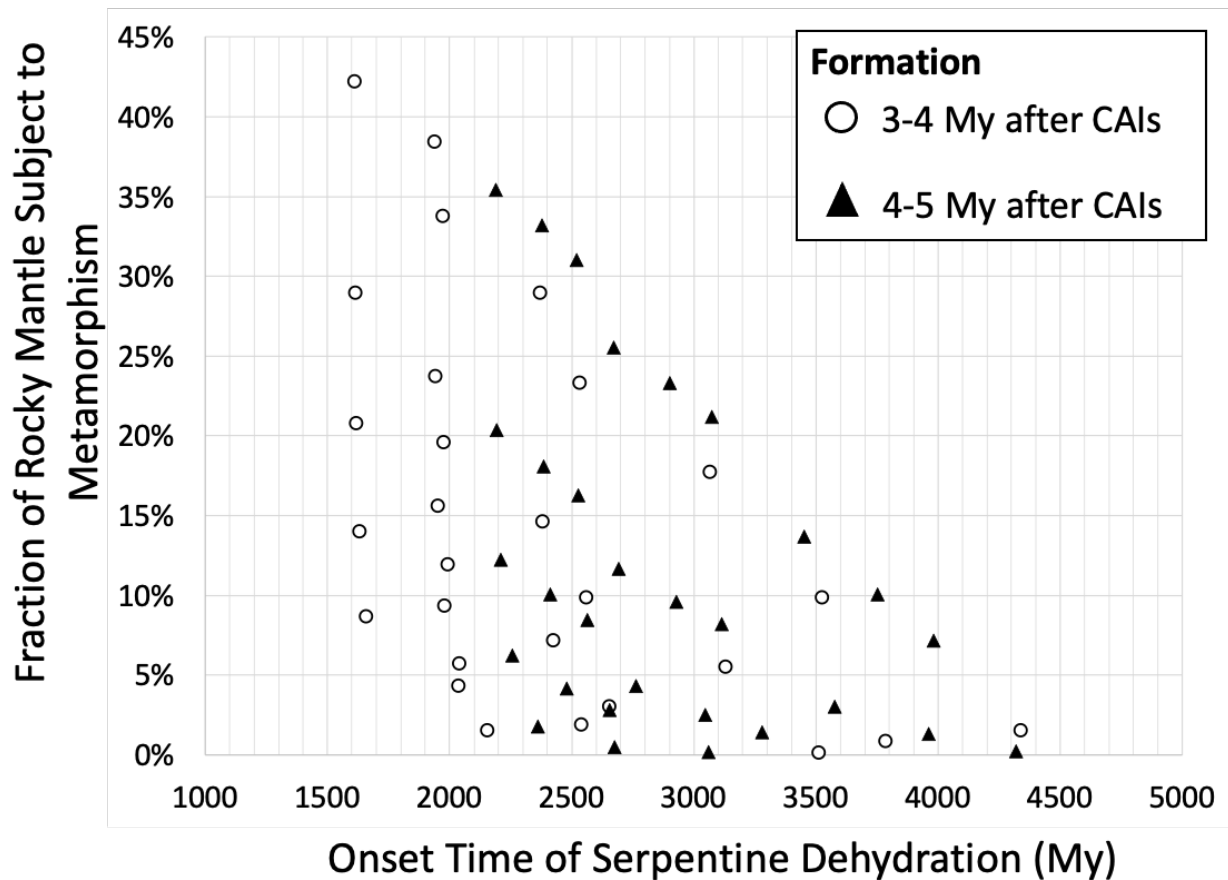


**Figure C.1.** Onset time and extent of thermal metamorphism (dehydration of serpentine) in Titania’s rocky core, assuming the moon accreted from chondritic material for various conditions (time of formation with respect to CAIs, rocky core thermal conductivity).

## REFERENCES

- Allen, P. A., Allen, J. R. (2005) *Basin Analysis: Principles and Application to Petroleum Play Assessment, Second Edition*, Blackwell Publishing Ltd., Oxford, 549 pp.
- Altair, T., de Avellar, M. G. B., Rodrigues, F., Galante, D. (2018) Microbial habitability of Europa sustained by radioactive sources. *Scientific Reports* 8. doi:10.1038/s41598-017-18470-z
- Andrade, E. N. D. C. (1910). On the viscous flow in metals, and allied phenomena. *Proceedings of the Royal Society of London. Series A, Containing Papers of a Mathematical and Physical Character*, 84(567), 1-12.

- Archie, G. E. (1942). The electrical resistivity log as an aid in determining some reservoir characteristics. *Transactions of the AIME*, 146(01), 54-62.
- Archinal, B.A., Acton, C.H., A’Hearn, M.F. et al. Report of the IAU Working Group on Cartographic Coordinates and Rotational Elements: 2015. *Celest Mech Dyn Astr* 130, 22 (2018). <https://doi.org/10.1007/s10569-017-9805-5>
- Arridge, C. S., Eggington, J. W. B. (2021) Electromagnetic induction in the icy satellites of Uranus, *Icarus* 367, 114562. <https://doi.org/10.1016/j.icarus.2021.114562>
- Bardyn, A. and 25 colleagues (2017) Carbon-rich dust in comet 67P/Churyumov-Gerasimenko measured by COSIMA/Rosetta. *Monthly Notices of the Royal Astronomical Society* 469, S712–S722. doi:10.1093/mnras/stx2640
- Bauer, J.M., Roush, T.L., Geballe, T.R., Meech, K.J., Owen, T.C., Vacca, W.D., Rayner, J.T. and Jim, K.T., 2002. The near infrared spectrum of Miranda: Evidence of crystalline water ice. *Icarus*, 158(1), pp.178-190.
- Beddingfield, C. B., D. M. Burr, and J. P. Emery (2015) "Fault geometries on Uranus' satellite Miranda: Implications for internal structure and heat flow." *Icarus* 247 (2015): 35-52.
- Beddingfield, C.B. and Cartwright, R.J., 2021. A lobate feature adjacent to a double ridge on Ariel: Formed by cryovolcanism or mass wasting?. *Icarus*, p.114583.
- Beddingfield, C.B., R.J. Cartwright, E.J. Leonard, T. Nordheim, F. Scipioni (2022a) Ariel's elastic thicknesses and heat fluxes, *Planetary Science Journal* 3, 106.
- Beddingfield, C.B., E. Leonard, R.J. Cartwright, C. Elder, T. Nordheim (2022b, under review) "High heat flux near Miranda's Inverness Corona consistent with a geologically recent heating event", *Planetary Science Journal*, under review.
- Beziat, A. (1988) Effect of Compaction Pressure and Water Content on the Thermal Conductivity of Some Natural Clays. *Clays and Clay Minerals* 36, 462–466. doi:10.1346/CCMN.1988.0360512
- Bierson, C., Nimmo, F. (2022) A note on the possibility of subsurface oceans on the uranian satellites, *Icarus*, 373, 114776, <https://doi.org/10.1016/j.icarus.2021.114776>
- Bland, P. A., Travis, B. J. (2017) Giant convecting mud balls of the early solar system. *Science Advances*, 3, e1602514.
- Bland, M. T., Nordheim, T. A., Patthoff, D. A., Vance, S. D. (2022) Elevated heat flux on Uranus' moon Ariel inferred from its largest observed impact crater, *Lunar and Planetary Science Conference* 53, 1140.
- Boström, M., Estes, V., Fiedler, J., Brevik, I., Buhmann, S. Y., Persson, C., et al. (2021). Self-preserving ice layers on CO<sub>2</sub> clathrate particles: Implications for Enceladus, Pluto, and similar ocean worlds. *Astronomy & Astrophysics*, 650, A54. <https://doi.org/10.1051/0004-6361/202040181>

- Bouquet, A. Glein, C. R., Wyrick, D., Waite, J. H. (2017) Alternative energy: Production of  $H_2$  by radiolysis of water in the rocky cores of icy bodies. *Astrophysical Journal Letters*, 840:L8.
- Bowling, T. J., Ciesla, F. J., Davison, T. M., Scully, J. E. C., Castillo-Rogez, J. C., Marchi, S. (2019) Post-Impact Thermal Structure and Cooling Timescales of Occator Crater on Asteroid 1 Ceres. *Icarus* 320:110-118, <https://doi.org/10.1016/j.icarus.2018.08.028>.
- Bradshaw, A. and Schleicher, K. (1980). Electrical conductivity of seawater. *IEEE Journal of Oceanic Engineering* 5, 50-62. <https://doi.org/10.1109/JOE.1980.1145449>
- Bridges, J.C. and Schwenzer, S.P. (2012). The nakhlite hydrothermal brine on Mars. *Earth and Planetary Science Letters* 359, 117-123. <https://doi.org/10.1016/j.epsl.2012.09.044>
- Carnahan, E., Vance, S. D., Hesse, M. A., Journaux, B., & Sotin, C. (2022). Dynamics of mixed clathrate-ice shells on ocean worlds. *Geophysical Research Letters*, 49, e2021GL097602. <https://doi.org/10.1029/2021GL097602>
- Cartwright, R.J., Emery, J.P., Rivkin, A.S., Trilling, D.E. and Pinilla-Alonso, N., 2015. Distribution of  $CO_2$  ice on the large moons of Uranus and evidence for compositional stratification of their near-surfaces. *Icarus*, 257, pp.428-456.
- Cartwright, R.J., Emery, J.P., Pinilla-Alonso, N., Lucas, M.P., Rivkin, A.S. and Trilling, D.E., 2018. Red material on the large moons of Uranus: Dust from the irregular satellites?. *Icarus*, 314, pp.210-231.
- Cartwright, R.J., Beddingfield, C.B., Nordheim, T.A., Roser, J., Grundy, W.M., Hand, K.P., Emery, J.P., Cruikshank, D.P. and Scipioni, F. (2020). Evidence for ammonia-bearing species on the Uranian satellite Ariel supports recent geologic activity. *The Astrophysical Journal Letters*, 898(1), L22.
- Cartwright, R.J., Beddingfield, C.B., Nordheim, T.A., Elder, C.M., Castillo-Rogez, J.C., Neveu, M., Bramson, A.M., Sori, M.M., Buratti, B.J., Pappalardo, R.T. and Roser, J.E., 2021. The science case for spacecraft exploration of the Uranian satellites: Candidate ocean worlds in an ice giant system. *Planetary Science Journal* 2, 120.
- Cartwright, R.J., Nordheim, T.A., DeColibus, D.R., Grundy, W.M., Holler, B.J., Beddingfield, C.B., Sori, M.M., Lucas, M.P., Elder, C.M., Regoli, L.H., Cruikshank, D.P., Emery, J.P., Leonard, E.J., and Cochrane, C.J., 2022. A  $CO_2$  cycle on Ariel? Radiolytic production and migration to low latitude cold traps. *Planetary Science Journal* 3, 8.
- Castillo-Rogez, J.C., Matson, D.L., Sotin, C., Johnson, T.V., Lunine, J.I., Thomas, P.C. (2007). Iapetus' geophysics: Rotation rate, shape, and equatorial ridge. *Icarus* 190:179-202. <https://doi.org/10.1016/j.icarus.2007.02.018>
- Castillo-Rogez, J. C., Johnson, T. V., Lee, M. H., Turner, N., Lunine, J. I., Matson, D. L. (2009)  $^{26}Al$  decay: Heat production and a revised age for Iapetus,



- Icarus 204, 658-662, doi:10.1016/j.icarus.2009.07.025.
- Castillo-Rogez, J. C., Efroimsky, M., Lainey, V., The tidal history of Iapetus. Dissipative spin dynamics in the light of a refined geophysical model, *J. Geophys. Res.* 116, E09008, doi:10.1029/2010JE003664.
- Castillo-Rogez, J. C., Hesse, M., et al. (2019) Conditions for the preservations of brines inside Ceres, to *Geophysical Research Letters* , 46, 1963-1972.
- Castillo, J. C. (2020) Future exploration of Ceres as an ocean world, *Nature Astronomy, News and Views* 4, 732-734.
- Castillo-Rogez, J. C., et al., Role of Supervolatiles in Driving Ocean Salinity and Electrical Conductivity in Ocean Worlds, *Geophysical Research Letters*, accepted. <https://doi.org/10.1002/essoar.10509076.1>
- Charnoz, S., Crida, A., Castillo-Rogez, J., Lainey, V., Dones, L., Accretion of Saturn's mid-sized moons during the viscous spreading of young massive rings: solving the paradox of silicate-poor rings versus silicate-rich moons, *Icarus* 210, 635-643, doi: 10.1016/j.icarus.2010.08.005.
- Chen, E. M. A., Nimmo, F., Glatzmaier, G. A. (2014) Tidal heating in icy satellite oceans, *Icarus* 229, 11-30. doi:10.1016/j.icarus.2013.10.024
- Choblet, G., Tobie, G., Sotin, C., Behoukova, M., Cadek, O., Postberg, F., Soucek, O. (2017) Powering prolonged hydrothermal activity inside Enceladus, *Nature Astronomy*, doi: 10.1038/s41550-017-0289-8.
- Clarke, A. (2014) The thermal limits to life. *International Journal of Astrobiology* 13:141–154.
- Cochrane, C. J., Persinger, R. R., Vance, S. D., Midkiff, E. L., Castillo-Rogez, J., Luspay-Kuti, A., et al. (2022). Single- and multi-pass magnetometric sub-surface ocean detection and characterization in icy worlds using Principal Component Analysis (PCA): Application to Triton. *Earth and Space Science*, 9, e2021EA002034. <https://doi.org/10.1029/2021EA002034>
- Cockell, C.S., T. Bush, C. Bryce, S. Direito, M. Fox-Powell, J.P. Harrison, H. Lammer, H. Landenmark, J. Martin-Torres, N. Nicholson, L. Noack, J. O'Malley-James, S.J. Payler, A. Rushby, T. Samuels, P. Schwendner, J. Wadsworth, and M.P. Zorzano. *Astrobiology*. Jan 2016.89-117.<http://doi.org/10.1089/ast.2015.1295>.
- Cong, L. She, X., Leng, G., Qiao, G., Li, C., Ding, Y. (2019) Formulation and Characterisation of Ternary Salt Based Solutions as Phase Change Materials for Cold Chain Applications, *Energy Procedia* 158, 5103-5108, <https://doi.org/10.1016/j.egypro.2019.01.690>.
- Connolly JAD (2005) Computation of phase equilibria by linear programming: A tool for geodynamic modeling and its application to subduction zone decarbonation. *Earth and Planetary Science Letters* 236:524–541. <https://doi.org/10.1016/j.epsl.2005.04.033>

- Connolly JAD (2009) The geodynamic equation of state: What and how. *Geochemistry, Geophysics, Geosystems* 10:Q10014. <https://doi.org/10.1029/2009GC002540>
- Connolly JAD, Galvez ME (2018) Electrolytic fluid speciation by Gibbs energy minimization and implications for subduction zone mass transfer. *Earth and Planetary Science Letters* 501:90–102. <https://doi.org/10.1016/j.epsl.2018.08.024>
- Crida, A., & Charnoz, S. (2012). Formation of regular satellites from ancient massive rings in the solar system. *Science*, 338(6111), 1196–1199.
- Croft, S. K., and L. A. Soderblom. (1991) Geology of the Uranian satellites. in *Uranus*, Eds. J. T. Bergstrahl, E. D. Miner, M. S. Matthews, The University of Arizona Space Science Series, 561–628.
- Cruikshank, D.P., Umurhan, O.M., Beyer, R.A., Schmitt, B., Keane, J.T., Runyon, K.D., Atri, D., White, O.L., Matsuyama, I., Moore, J.M. and McKinnon, W.B., 2019. Recent cryovolcanism in virgil fossae on Pluto. *Icarus*, 330, pp.155–168.
- Cuk, M., El Moutamid, M., Tiscareno, M. S. (2020) Dynamical history of the Uranian system, *Planetary Science Journal* 1 22, <https://doi.org/10.3847/PSJ/ab9748>
- Daigle, H., Screaton, E. J. (2015) Evolution of sediment permeability during burial and subduction, *Geofluids* 15, 84–105.  
<https://onlinelibrary.wiley.com/doi/epdf/10.1111/gfl.12090>
- De Sanctis, M. C., Mitri, G., Castillo-Rogez, J., House, C. H., Marchi, S., Raymond, C. A., & Sekine, Y. (2020). Relict ocean worlds: Ceres. *Space Science Reviews*, 216(4), 1–33.
- Desch, S. J., Kalyaan, A., & Alexander, C. M. D. (2018). The effect of Jupiter’s formation on the distribution of refractory elements and inclusions in meteorites. *The Astrophysical Journal Supplement Series*, 238(1), 11.
- Dhooghe, F., De Keyser, J., Altwegg, K., Briois, C., Balsiger, H., Berthelier, J.J., Calmonte, U., Cessateur, G., Combi, M.R., Equeter, E. and Fiethé, B., 2017. Halogens as tracers of protosolar nebula material in comet 67P/Churyumov–Gerasimenko. *Monthly Notices of the Royal Astronomical Society*, 472(2), pp.1336–1345.
- Eluszkiewicz, J., & Leliwa-Kopystyński, J. (1989). Compression effects in rock-ice mixtures: an application to the study of satellites. *Physics of the Earth and Planetary Interiors*, 55(3–4), 387–398.
- Engel, S., Lunine, J.I. and Norton, D.L., 1994. Silicate interactions with ammonia-water fluids on early Titan. *Journal of Geophysical Research: Planets*, 99, pp.3745–3752.
- Ermakov, A., Fu, R. R., Castillo-Rogez, J. C., et al. (2017) Constraints on Ceres’ internal structure and evolution from its shape and gravity measured the Dawn spacecraft, *Journal of Geophysical Research*, 122, 2267–2293.

- Fuller, J., Luan, J., Quataert, E. (2016) Resonance locking as the source of rapid tidal migration in the Jupiter and Saturn moon systems. *Monthly Notices of the Royal Astronomical Society*, 458, 3867–3879. doi:10.1093/mnras/stw609
- Galvez ME, Manning CE, Connolly JAD, Rumble D (2015) The solubility of rocks in metamorphic fluids: A model for rock-dominated conditions to upper mantle pressure and temperature. *Earth and Planetary Science Letters*, 430, 486–498. <https://doi.org/10.1016/j.epsl.2015.06.019>
- Glover, P.W.J., Gomez, J.B., Meredith, P.G., Hayashi, K., Sammonds, P.R. and Murrell, S.A.F., 1997. Damage of saturated rocks undergoing triaxial deformation using complex electrical conductivity measurements: experimental results. *Physics and Chemistry of the Earth*, 22(1-2), 57-61.
- Grundy, W.M., Young, L.A. and Young, E.F., 2003. Discovery of CO<sub>2</sub> ice and leading–trailing spectral asymmetry on the uranian satellite Ariel. *Icarus*, 162(1), pp.222-229.
- Grundy, W.M., Young, L.A., Spencer, J.R., Johnson, R.E., Young, E.F. and Buie, M.W., 2006. Distributions of H<sub>2</sub>O and CO<sub>2</sub> ices on Ariel, Umbriel, Titania, and Oberon from IRTF/SpeX observations. *Icarus*, 184(2), pp.543-555.
- Grundy, W.M., Binzel, R.P., Buratti, B.J., Cook, J.C., Cruikshank, D.P., Dalle Ore, C.M., Earle, A.M., Ennico, K., Howett, C.J.A., Lunsford, A.W. and Olkin, C.B., 2016. Surface compositions across Pluto and Charon. *Science*, 351, aad9189.
- Hammond, N.P., Barr, A.C. (2014). Global resurfacing of Uranus’s moon Miranda by convection. *Geology* 42:931-934. <https://doi.org/10.1130/G36124.1>
- Hand, K. P., Carlson, R. W., Chyba, C. F. (2007) Energy, Chemical Disequilibrium, and Geological Constraints on Europa. *Astrobiology*, 7, 1006–1022. doi:10.1089/ast.2007.0156
- Hanel R, Conrath B, Flasar FM, Kunde V, Maguire W, Pearl J, Pirraglia J, Samuelson R, Cruikshank D, Gautier D, Gierasch P. Infrared observations of the Uranian system. *Science*. 1986 Jul 4;233(4759):70-4.
- He, R., Jia, N., Jin, H., Wang, H., Li, X. (2021) Experimental study on thermal conductivity of organic-rich soils under thawed and frozen states, *Geofluids* 2021, 7566669, <https://doi.org/10.1155/2021/7566669>
- Helled, R. and Bodenheimer, P., 2014. The formation of Uranus and Neptune: challenges and implications for intermediate-mass exoplanets. *The Astrophysical Journal*, 789(1), p.69.
- Helled, R., Nettelmann, N. & Guillot, T. Uranus and Neptune: Origin, evolution and internal structure. *Space Science Reviews*, 216, 38 (2020). <https://doi.org/10.1007/s11214-020-00660-3>
- Hemingway, D.J., Mittal, T. (2019) Enceladus’s ice shell structure as a window on internal heat production. *Icarus*, 332, 111-131. <https://doi.org/10.1016/j.icarus.2019.03.011>

- Hendrix, A.R., Hurford, T.A., Barge, L.M., Bland, M.T., Bowman, J.S., Brinckerhoff, W., Buratti, B.J., Cable, M.L., Castillo-Rogez, J., Collins, G.C. and Diniega, S., 2019. The NASA roadmap to ocean worlds. *Astrobiology*, 19, pp.1-27.
- Herbert, F., 2009. Aurora and magnetic field of Uranus. *Journal of Geophysical Research: Space Physics*, 114(A11).
- Hesselbrock, A.J. and Minton, D.A., 2019. Three dynamical evolution regimes for coupled ring-satellite systems and implications for the formation of the Uranian Satellite Miranda. *The Astronomical Journal*, 157, p.30.
- Hillier, J., Squyres, S. W. (1991) Thermal stress tectonics on the satellites of Saturn and Uranus. *Journal of Geophysical Research: Planets*, 96, 15665-15674.
- Hussmann, H., Sohl, F., Spohn, T. (2006) Subsurface oceans and deep interiors of medium-sized outer planet satellites and large trans-neptunian objects, *Icarus* 185, 258-273.
- Horne, R.A. and Frysinger, G.R. (1963) The effect of pressure on the electrical conductivity of sea water. *Journal of Geophysical Research* 68, 1967-1973. <https://doi.org/10.1029/JZ068i007p01967>
- Ida, S., Ueta, S., Sasaki, T., & Ishizawa, Y. (2020). Uranian satellite formation by evolution of a water vapour disk generated by a giant impact. *Nature Astronomy*, 4, 880-885.
- Jacobson, R. A. (2014). The orbits of the Uranian satellites and rings, the gravity field of the Uranian system, and the orientation of the pole of Uranus. *The Astronomical Journal*, 148, 76.
- Janes, D. M., and Melosh, H. J. (1988), Sinkers tectonics: An approach to the surface of Miranda, *Journal of Geophysical Research: Planets*, 93, 3127– 3143, doi:10.1029/JB093iB04p03127 .
- Jellison, R., MacIntyre, S., & Millero, F. J. (1999). Density and conductivity properties of Na– CO<sub>3</sub>– Cl– SO<sub>4</sub> brine from Mono Lake, California, USA. *International Journal of Salt Lake Research*, 8(1), 41-53.
- Kamata, S., Nimmo, F., Sekine, Y., Kuramoto, K., Noguchi, N., Kimura, J., Tani, A. (2019) Pluto's ocean is capped and insulated by gas hydrates, *Nature Geoscience* 12, 407-410.
- Kargel, J. S. (1991). Brine volcanism and the interior structures of asteroids and icy satellites. *Icarus*, 94, 368-390.
- Kargel, J. S. (1998). Physical Chemistry of Ices in the Outer Solar System. In *Solar System Ices* , pp. 3-32. Springer, Dordrecht.
- Kegerreis, J.A., Teodoro, L.F.A., Eke, V.R., Massey, R.J., Catling, D.C., Fryer, C.L., Korycansky, D.G., Warren, M.S. and Zahnle, K.J., 2018. Consequences of giant impacts on early Uranus for rotation, internal structure, debris, and atmospheric erosion. *The Astrophysical Journal*, 861, p.52.

- Kim, C., Lee, Y., Lee, E. Y. (2018) Numerical analysis of sedimentary compaction: Implications for porosity and layer thickness variation, *Journal of the Geological Society of Korea*, 54, 631-640, <https://doi.org/10.14770/jgsk.2018.54.6.631>
- King, S. D., Bland, M. T., Marchi, S., Raymond, C. A., Russell, C. T., Scully, J. E. C., & Sizemore, H. G. (2022). Ceres' broad-scale surface geomorphology largely due to asymmetric internal convection. *AGU Advances*, 3, e2021AV000571. <https://doi.org/10.1029/2021AV000571>
- Kirchoff, M., L. Dones, K. Singer, P. Schenk (2022) "Crater distributions of Uranus' mid-sized satellites and implications for outer solar system bombardment" *Planetary Science Journal*, in press.
- Lambrechts, M., Johansen, A., Morbidell, A. (2014) Separating gas-giant and ice-giant planets by halting pebble accretion. *Astronomy & Astrophysics*, 572, A35.
- Le Roy, L., Altwegg, K., Balsiger, H., Berthelier, J.J., Bieler, A., Briois, C., Calmonte, U., Combi, M.R., De Keyser, J., Dhooghe, F. and Fiethe, B., 2015. Inventory of the volatiles on comet 67P/Churyumov-Gerasimenko from Rosetta/ROSINA. *Astronomy & Astrophysics*, 583, p.A1.
- Livingston, F. E., Smith, J. A., & George, S. M. (2002). General trends for bulk diffusion in ice and surface diffusion on ice. *The Journal of Physical Chemistry A*, 106, 6309-6318.
- Lodders, K., 2021. Relative atomic solar system abundances, mass fractions, and atomic masses of the elements and their isotopes, composition of the solar photosphere, and compositions of the major chondritic meteorite groups. *Space Science Reviews*, 217, 1-33.
- Mao, X. and McKinnon, W.B., 2018. Faster paleospin and deep-seated uncompensated mass as possible explanations for Ceres' present-day shape and gravity. *Icarus*, 299, 430-442.
- Marion, G.M., Mironenko, M.V. and Roberts, M.W., 2010. FREZCHEM: A geochemical model for cold aqueous solutions. *Computers & Geosciences*, 36(1), pp.10-15.
- Marion, G. M., Kargel, J. S., Catling, D. C., & Lunine, J. I. (2012). Modeling ammonia-ammonium aqueous chemistries in the Solar System's icy bodies. *Icarus*, 220, 932-946.
- Martin, B., Fyfe, W. S. (1970). Some experimental and theoretical observations on the kinetics of hydration reactions with particular reference to serpentinization. *Chemical Geology*, 6, 185-202.
- Matson D. L., Castillo-Rogez J. C., McKinnon W. B., Sotin C., Schubert G., The thermal evolution and internal structure of Saturn's midsize icy satellites, In: Saturn after Cassini-Huygens, Eds: R. Brown, M. Dougherty, L. Esposito, T. Krimigis, H. Waite, Chapter 19, doi: 10.1007/978-1-4020-9217-6\_18

- McCleskey, R. B., Nordstrom, D. K., Ryan, J. N. (2012) Comparison of electrical conductivity calculation methods for natural waters, *Limnology and Oceanography, Methods* 10, 952-967, <https://doi.org/10.4319/lom.2012.10.952>
- McKinnon, W. B. (2013), The shape of Enceladus as explained by an irregular core: Implications for gravity, libration, and survival of its sub-surface ocean, *Journal of Geophysical Research: Planets*, 118, 1775– 1788, doi:10.1002/jgre.20122.
- Melwani Daswani, M. and Castillo-Rogez, J.C., 2022. Porosity-filling Metamorphic Brines Explain Ceres’s Low Mantle Density. *The Planetary Science Journal*, 3(1), p.21.
- Melwani Daswani, M., Vance, S. D., Mayne, M. J., & Glein, C. R. (2021). A metamorphic origin for Europa’s Ocean. *Geophysical Research Letters*, 48, e2021GL094143. <https://doi.org/10.1029/2021GL094143>.
- Moore, M.H., Ferrante, R.F., Hudson, R.L. and Stone, J.N., 2007. Ammonia–water ice laboratory studies relevant to outer solar system surfaces. *Icarus*, 190, pp.260-273.
- Nesvorný, D. and Morbidelli, A., 2012. Statistical study of the early solar system’s instability with four, five, and six giant planets. *The Astronomical Journal*, 144, p.117.
- Morbidelli, A., Tsiganis, K., Batygin, K., Crida, A. and Gomes, R., 2012. Explaining why the uranian satellites have equatorial prograde orbits despite the large planetary obliquity. *Icarus*, 219(2), pp.737-740.
- Mousis O., Aguichine A., Helled R., Irwin P. G. J. and Lunine J. I. (2020) The role of ice lines in the formation of Uranus and Neptune, *Phil. Trans. R. Soc. A*.3782020010720200107 <http://doi.org/10.1098/rsta.2020.0107>
- NASEM - National Academies of Sciences, Engineering, and Medicine. 2022. *Origins, Worlds, and Life: A Decadal Strategy for Planetary Science and Astrobiology 2023-2032*. Washington, DC: The National Academies Press. <https://doi.org/10.17226/26522>.
- Néri, A., Guyot, F., Reynard, B., & Sotin, C. (2020). A carbonaceous chondrite and cometary origin for icy moons of Jupiter and Saturn. *Earth and Planetary Science Letters*, 530, 115920.
- Neveu, M., & Desch, S. J. (2015). Geochemistry, thermal evolution, and cryo-volcanism on Ceres with a muddy ice mantle. *Geophysical Research Letters*, 42, 10-197.
- Neveu, M., Desch, S. J., & Castillo-Rogez, J. C. (2015). Core cracking and hydrothermal circulation can profoundly affect Ceres’ geophysical evolution. *Journal of Geophysical Research: Planets*, 120, 123-154.
- Neveu, M., Desch, S., Castillo-Rogez, J. (2017) Aqueous chemistry in icy world interiors: Fate of antifreeze and radionuclides, *Geochimica and Cosmochimica*

*Acta* 212, 324-371.

Neveu, M. and Rhoden, A.R. (2019) Evolution of Saturn's mid-sized moons, *Nature Astronomy* 3, 543-552.

Neumann, W., Kruse, A. (2019). Differentiation of Enceladus and retention of a porous core. *The Astrophysical Journal*, 882(1), 47.

Neumann, W., Jaumann, R., Castillo-Rogez, J. C., Raymond, C. A., Russell, C. T. (2020) Ceres' Partial Differentiation: Undifferentiated Crust Mixing with a Water-Rich Mantle, *A&A* 633, id. A117.

Obradors-Prats, J., Rouainia, M., Aplin, A. C., & Crook, A. J. L. (2019). A diagenesis model for geomechanical simulations: Formulation and implications for pore pressure and development of geological structures. *Journal of Geophysical Research: Solid Earth*, 124, 4452–4472. <https://doi.org/10.1029/2018JB016673>

Oldenborger, G. A. (2021) Subzero temperature dependence of electrical conductivity for permafrost geophysics, *Cold Regions Science and Technology*, 182, 103214. <https://doi.org/10.1016/j.coldregions.2020.103214>

Opeil, C. P., Consolmagno, G. J., Britt, D. T. (2010) The thermal conductivity of meteorites: New measurements and analysis. *Icarus*, 208, 449-454.

Opeil, C.P., Britt, D.T., Macke, R.J., Consolmagno, G.J. (2020) The surprising thermal properties of CM carbonaceous chondrites. *Meteoritics & Planetary Science*, 55(8).

Palme, H., Lodders, K., & Jones, A. (2014). Solar system abundances of the elements. Planets, Asteroids, Comets and The Solar System, Volume 2 of *Treatise on Geochemistry* (Second Edition). Edited by Andrew M. Davis. Elsevier, 2014., p. 15-36, 2.

Pan, Y., Yong, W., & Secco, R. A. (2021). Electrical conductivity of aqueous NaCl at high pressure and low temperature: Application to deep subsurface oceans of icy moons. *Geophysical Research Letters*, 48, e2021GL094020. <https://doi.org/10.1029/2021GL094020>

Pappalardo, R. T., Reynolds, S. J., and Greeley, R. (1997), Extensional tilt blocks on Miranda: Evidence for an upwelling origin of Arden Corona, *Journal of Geophysical Research*, 102( E6), 13369– 13379, doi:10.1029/97JE00802.

Park, R.S., Konopliv, A.S., Bills, B.G., Rambaux, N., Castillo-Rogez, J.C., Raymond, C.A., Vaughan, A.T., Ermakov, A.I., Zuber, M.T., Fu, R.R. and Toplis, M.J., 2016. A partially differentiated interior for (1) Ceres deduced from its gravity field and shape. *Nature*, 537, 515-517.

Pätzold, M., Andert, T., Hahn, M., Asmar, S. W., Barriot, J. P., Bird, M. K., ... & Scholten, F. (2016). A homogeneous nucleus for comet 67P/Churyumov–Gerasimenko from its gravity field. *Nature*, 530, 63-65.

- Pavlov, T., Vlahovic, L., Staicu, D., Konings, R. J. M., Wenman, M. R., Van Uffelen, P., & Grimes, R. W. (2017). A new numerical method and modified apparatus for the simultaneous evaluation of thermo-physical properties above 1500 K: A case study on isostatically pressed graphite. *Thermochimica Acta*, 652, 39-52.
- Peterson et al. (2015) Postberg, F., Schmidt, J., Hillier, J., Kempf, S., Srama, R. (2011) A salt-water reservoir as a source of compositionally stratified plume on Enceladus, *Nature* 474, 620-622.
- Protopapa, S., Cook, J. C., Grundy, W. M., Cruikshank, D. P., Dalle Ore, C. M., & Beyer, R. A. (2021). Surface Composition of Charon. *The Pluto System After New Horizons*, Arizona University Press, Tucson, AZ, 433.
- Qi, C., Stern, L. A., Pathare, A., Durham, W. B., & Goldsby, D. L. (2018). Inhibition of grain boundary sliding in fine-grained ice by intergranular particles: Implications for planetary ice masses. *Geophysical Research Letters*, 45, 12-757.
- Raponi, M.C. De Sanctis, F.G. Carrozzo, M. Ciarniello, J.C. Castillo-Rogez, E. Ammannito, A. Frigeri, A. Longobardo, E. Palomba, F. Tosi, F. Zambon, C.A. Raymond, C.T. Russell (2019) Mineralogy of Occator crater on Ceres and insight into its evolution from the properties of carbonates, phyllosilicates, and chlorides. *Icarus* 320, 83-96, doi:10.1016/j.icarus.2018.02.001.
- Ray, C., Glein, C.R., Waite, J.H., Teolis, B., Hoehler, T., Huber, J.A., Lunine, J. and Postberg, F., 2021. Oxidation processes diversify the metabolic menu on Enceladus. *Icarus*, 364, p.114248.
- Rebello, L. R. R., Siepmann, T., Drexler, S. (2020) Correlations between TDS and electrical conductivity for high-salinity formation brines characteristic of South Atlantic pre-salt basins, *Water SA* 46, 602-609, <https://doi.org/10.17159/wsa/2020.v46.i4.9073>
- Renaud, J.P., Henning, W.G., Saxena, P., Neveu, M., Bagheri, A., Mandell, A., Hurford, T. (2021) Tidal Dissipation in Dual-body, Highly Eccentric, and Nonsynchronously Rotating Systems: Applications to Pluto–Charon and the Exoplanet TRAPPIST-1e. *The Planetary Science Journal* 2, 4. <https://doi.org/10.3847/PSJ/abc0f3>
- Revil, A., Cathles III, L. M., Losh, S., & Nunn, J. A. (1998). Electrical conductivity in shaly sands with geophysical applications. *Journal of Geophysical Research: Solid Earth*, 103, 23925-23936.
- Revil, A., & Glover, P. W. J. (1998). Nature of surface electrical conductivity in natural sands, sandstones, and clays. *Geophysical Research Letters*, 25, 691-694.
- Roberts, J.~H. (2015) The fluffy core of Enceladus. *Icarus* 258, 54–66. doi:10.1016/j.icarus.2015.05.033
- Salmon, J. and Canup, R.M., 2022. Co-accretion + giant impact origin of the Uranus system: Post-impact evolution. *The Astrophysical Journal*, 924, p.6.



Saner, S., & Kissami, M. (2003). Critical salinity for Archie–non Archie models in the Jauf Sandstone reservoir, Saudi Arabia. In Proceedings SCA Intl. Symposium.

Schenk, P. M., Moore, J. M. (2020) Topography and geology of Uranian mid-sized icy satellites in comparison with Saturnian and Plutonian satellites, *Philosophical Transactions of the Royal Society of London A*, 378, <http://doi.org/10.1098/rsta.2020.0102>

Schmidt, C. and Manning, C. (2017) Pressure-induced ion pairing in  $\text{MgSO}_4$  solutions: Implications for the oceans of icy worlds, *Geochemical Perspectives Letters*, 3:66–74.

Scully, J., Schenk, P., Castillo-Rogez, J., et al. (2020) The varied sources of faculae-forming brines in Ceres’ Occator crater, emplaced via brine effusion in a hydrothermal system, *Nature Communications* 11, id. 3680.

Shoshany, Y., Prialnik, D., & Podolak, M. (2002). Monte Carlo modeling of the thermal conductivity of porous cometary ice. *Icarus*, 157, 219–227.

Slack, G. A. (1980). Thermal conductivity of ice. *Physical Review B*, 22, 3065.

Sloan, E. D., & Koh, C. A. (2008). *Clathrate Hydrates of Natural Gases* (3. ed). Boca Raton, FL: CRC Press, Taylor & Francis.

Smith, S. H. (1962) Temperature correction in conductivity measurements, *Limnology and Oceanography* 7, 330–334, doi: [10.4319/lo.1962.7.3.0330](https://doi.org/10.4319/lo.1962.7.3.0330)

Smith, B.A., Soderblom, L.A., Beebe, R., Bliss, D., Boyce, J.M., Brahic, A., Briggs, G.A., Brown, R.H., Colli

Stern, R. J., Gerya, T., & Tackley, P. J. (2018). Stagnant lid tectonics: Perspectives from silicate planets, dwarf planets, large moons, and large asteroids. *Geoscience Frontiers*, 9(1), 103–119.

Szulágyi, J., Cilibrasi, M., Mayer, L. (2018) In situ formation of icy moons of Uranus and Neptune, *Astrophys. J. Lett.* 868 L13. <https://doi.org/10.3847/2041-8213/aaeed6>

Thomas, P.~C. (2010) Sizes, shapes, and derived properties of the saturnian satellites after the Cassini nominal mission. *Icarus* 208, 395–401. doi:10.1016/j.icarus.2010.01.025

Thommes, E., Duncan, M. & Levison, H. The formation of Uranus and Neptune in the Jupiter–Saturn region of the Solar System. *Nature* 402, 635–638 (1999). <https://doi.org/10.1038/45185>

Tittemore, W.C. and Wisdom, J. (1988). Tidal evolution of the Uranian satellites: I. Passage of Ariel and Umbriel through the 5: 3 mean-motion commensurability. *Icarus* 74, 172–230. [https://doi.org/10.1016/0019-1035\(88\)90038-3](https://doi.org/10.1016/0019-1035(88)90038-3)

Tortora, P., Zannoni, M., Hemingway, D., Nimmo, F., Jacobson, R.A., Iess, L. and Parisi, M., (2016) Rhea gravity field and interior modeling from Cassini data analysis, *Icarus* 264:264–273. <https://doi.org/10.1016/j.icarus.2015.09.022>

- Travis, B.J., Palguta, J., Schubert, G. (2012). A whole-moon thermal history model of Europa: Impact of hydrothermal circulation and salt transport. *Icarus* 218:1006-1019. <https://doi.org/10.1016/j.icarus.2012.02.008>
- Tyler, R. (2014) Comparative estimates of the heat generated by ocean tides on icy satellites in the outer Solar System, *Icarus* 243, 358-385, <https://doi.org/10.1016/j.icarus.2014.08.037>
- Ucok H., Ershaghi I., and Olhoeft G., (1980). Electrical resistivity of geothermal brines. *Journal of Petroleum Technology*, 32(04), 717-727.
- Ussher, G., Harvey, C., Johnstone, R., Anderson, E. (2000) Understanding the resistivities observed in geothermal systems, Proceedings World Geothermal Congress 2000, Kyushu - Tohoku, Japan, May 28 - June 10, 2000, 1915.
- Van Schmus, W.R., 1995. Natural radioactivity of the crust and mantle. In: Ahrens, T.J. (Ed.), A Handbook of Physical Constants: Global Earth Physics. In: AGU Reference Shelf Series, vol. 1. ISBN 0-87590-851-9. 380 pp.
- Weiss, B. P., Biersteker, J. B., Colicci, V., Goode, A., Castillo-Rogez, J. C., Petropoulos, A. E., Balint, T. S. (2021). Searching for subsurface oceans on the moons of Uranus using magnetic induction. *Geophysical Research Letters*, 48, e2021GL094758. <https://doi.org/10.1029/2021GL094758>
- Zahnle, K., Schenk, P., Levison, H. and Dones, L., 2003. Cratering rates in the outer Solar System. *Icarus*, 163(2), pp.263-289.
- Zandanel, A., Hellmann, R., Truche, L. et al. (2022) Geologically rapid aqueous mineral alteration at subfreezing temperatures in icy worlds. *Nature Astronomy*. <https://doi.org/10.1038/s41550-022-01613-2>
- Zharkov, V. N., Leontjev, V. V., Kozenko, A. V. (1985) Models, Figures, and Gravitational Moments of the Galilean Satellites of Jupiter and Icy Satellites of Saturn, *Icarus*, 61, 92-100.
- Zhu, D., Ciaia, P., Krinner, G. et al. (2019) Controls of soil organic matter on soil thermal dynamics in the northern high latitudes. *Nature Communications*, 10, 3172. <https://doi.org/10.1038/s41467-019-11103-1>
- Zolotov, M. Y., Shock, E. L. (2001). Composition and stability of salts on the surface of Europa and their oceanic origin. *Journal of Geophysical Research: Planets*, 106(E12), 32815-32827.